Dark Energy Survey Year 1 results: weak lensing shape catalogues

Dark Energy Survey Year 1 results: weak lensing shape catalogues

J. Zuntz,[1]* E. Sheldon,[2] S. Samuroff,[3] M. A. Troxel,[4,5] M. Jarvis,[6] N. MacCrann,[4,5]
D. Gruen,[7,8]† J. Prat,[9] C. Sánchez,[9] A. Choi,[4] S. L. Bridle,[3] G. M. Bernstein,[6]
S. Dodelson,[10,11] A. Drlica-Wagner,[10] Y. Fang,[6] R. A. Gruendl,[12,13] B. Hoyle,[14]
E. M. Huff,[15] B. Jain,[6] D. Kirk,[16] T. Kacprzak,[17] C. Krawiec,[6] A. A. Plazas,[15]
R. P. Rollins,[3] E. S. Rykoff,[7,8] I. Sevilla-Noarbe,[18] B. Soergel,[19,20] T. N. Varga,[14,21]
T. M. C. Abbott,[22] F. B. Abdalla,[16,23] S. Allam,[10] J. Annis,[10] K. Bechtol,[24]
A. Benoit-Lévy,[16,25,26] E. Bertin,[25,26] E. Buckley-Geer,[10] D. L. Burke,[7,8] A. Carnero
Rosell,[27,28] M. Carrasco Kind,[12,13] J. Carretero,[9] F. J. Castander,[29] M. Crocce,[29]
C. E. Cunha,[7] C. B. D'Andrea,[6] L. N. da Costa,[27,28] C. Davis,[7] S. Desai,[30] H. T. Diehl,[10]
J. P. Dietrich,[31,32] P. Doel,[16] T. F. Eifler,[15,33] J. Estrada,[10] A. E. Evrard,[34,35]
A. Fausti Neto,[27] E. Fernandez,[9] B. Flaugher,[10] P. Fosalba,[29] J. Frieman,[10,11]
J. García-Bellido,[36] E. Gaztanaga,[29] D. W. Gerdes,[34,35] T. Giannantonio,[14,19,20]
J. Gschwend,[27,28] G. Gutierrez,[10] W. G. Hartley,[16,17] K. Honscheid,[4,5] D. J. James,[37]
T. Jeltema,[38] M. W. G. Johnson,[13] M. D. Johnson,[13] K. Kuehn,[39] S. Kuhlmann,[40]
N. Kuropatkin,[10] O. Lahav,[16] T. S. Li,[10] M. Lima,[27,41] M. A. G. Maia,[27,28] M. March,[6]
P. Martini,[4,42] P. Melchior,[43] F. Menanteau,[12,13] C. J. Miller,[34,35] R. Miquel,[9,44]
J. J. Mohr,[21,31,32] E. Neilsen,[10] R. C. Nichol,[45] R. L. C. Ogando,[27,28] N. Roe,[46]
A. K. Romer,[47] A. Roodman,[7,8] E. Sanchez,[18] V. Scarpine,[10] R. Schindler,[8]
M. Schubnell,[35] M. Smith,[48] R. C. Smith,[22] M. Soares-Santos,[10] F. Sobreira,[27,49]
E. Suchyta,[50] M. E. C. Swanson,[13] G. Tarle,[35] D. Thomas,[45] D. L. Tucker,[10]
V. Vikram,[40] A. R. Walker,[22] R. H. Wechsler,[7,8,51] and Y. Zhang[10] (DES Collaboration)

Affiliations are listed at the end of the paper

ABSTRACT

We present two galaxy shape catalogues from the Dark Energy Survey Year 1 data set, covering 1500 deg^2 with a median redshift of 0.59. The catalogues cover two main fields: Stripe 82, and an area overlapping the South Pole Telescope survey region. We describe our data analysis process and in particular our shape measurement using two independent shear measurement pipelines, METACALIBRATION and IM3SHAPE. The METACALIBRATION catalogue uses a Gaussian model with an innovative internal calibration scheme, and was applied to *riz* bands, yielding 34.8M objects. The IM3SHAPE catalogue uses a maximum-likelihood bulge/disc model calibrated using simulations, and was applied to *r*-band data, yielding 21.9M objects. Both catalogues pass a suite of null tests that demonstrate their fitness for use in weak lensing science. We estimate the 1σ uncertainties in multiplicative shear calibration to be 0.013 and 0.025 for the METACALIBRATION and IM3SHAPE catalogues, respectively.

* E-mail: joe.zuntz@ed.ac.uk
† Einstein Fellow.

1 INTRODUCTION

Weak lensing, the gravitational bending of light paths by wide-field matter distributions, presents a powerful probe of cosmological physics and the laws of gravity. The angle by which light is bent by any lens depends on two factors: the geometry of the source–lens–observer system, and the inherent strength of the lens. In the cosmic case, the former depends on the expansion history of the Universe via the relationship between redshift and distance. The latter depends on laws of gravity and the amount of structure in the Universe – the variance of the cosmic density field. Through both these dependences we can put limits on the history of the Universe, the cosmological parameters, and most interestingly the behaviour of dark matter and the equation of state of dark energy.

The most direct way to measure weak lensing is to measure the ellipticity of distant galaxies. The effect of the intermediate gravitational fields on the light from a source is to shear it, coherently stretching the galaxies in a region in the same direction. The magnitude of this effect on a single galaxy is only a few per cent, which is much smaller than either the intrinsic scatter in galaxy shapes or the atmospheric and optical image distortion. The intrinsic scatter means we require large surveys, to obtain as much statistical power as possible, and the atmospheric and optical effects mean we require careful optical design and precision modelling of the induced distortions (the point spread function, PSF).

The Dark Energy Survey (DES) is the largest ongoing lensing survey designed to meet these requirements, and is part of the current 'Stage III' group of lensing surveys (Albrecht et al. 2006). The earliest Stage I surveys, including VIRMOS-Descart (Van Waerbeke, Mellier & Hoekstra 2005), CTIO (Jarvis et al. 2006), SDSS (Hirata et al. 2004), and COSMOS (Schrabback et al. 2007), mostly measured tens of square degrees, and made some of the first detections of cosmic shear. Stage II surveys included DLS (Jee et al. 2013), SDSS (Lin et al. 2012; Huff et al. 2014), RCSLenS (Hildebrandt et al. 2016), CFHTLenS (Heymans et al. 2012) as well as early science verification (SV) DES results in Jarvis et al. (2016). They included both deep and wide surveys, up to hundreds of square degrees, and obtained significant cosmological constraints. The current Stage III generation includes DES, KiDS (Hildebrandt et al. 2017; Amon et al. 2018), and HSC (Aihara et al. 2018), which are each surveying at least 1000 deg^2 and will obtain cosmological constraints comparable in power to all other cosmological data. Upcoming Stage IV surveys, including Euclid, LSST, WFIRST, and SKA, will measure the dark energy equation of state with 1 per cent precision when combined with data from the cosmic microwave background (CMB). DES will eventually survey 5000 deg^2. It has currently completed four out of its five planned full seasons of observations. The catalogues described in this paper use observations from the first of those 4 yr, and cover 1500 deg^2. Processing and analysis of the entirety of existing DES data is underway.

Building a catalogue of galaxy ellipticities (a shape catalogue) from image data is a long process with many steps, each of which must be performed with careful attention to potential induced biases. The DES implementation of these steps is shown visually in Fig. 1. The first stage is low-level calibration to detect artefacts, measure noise, and regularize images. We build coadded images and detect and classify stars and galaxies in them. We measure the astrometry and PSF in each single-epoch image. We collect together single-epoch 'postage-stamp' images for each source into a single
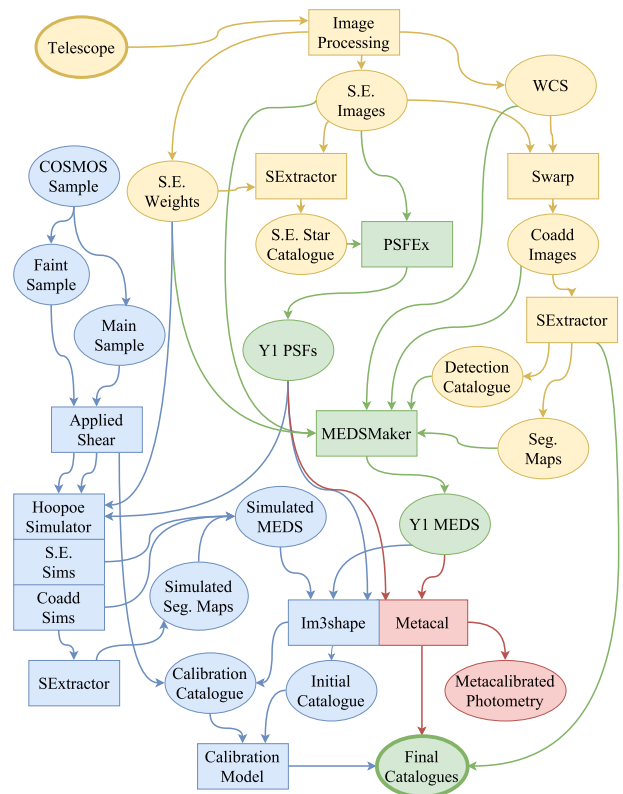
Figure 1. A flow-chart showing the steps in the DES Year 1 heckedshape analysis, starting from low-level calibrated data products made by DES Data Management (DES-DM) and ending with final output catalogues. Yellow stages are performed in the DES-DM software process. Green stages are performed in the Weak Lensing analysis process. Blue stages are part of the IM3SHAPE process, mostly simulation and calibration, and red stages part of the METACALIBRATION analysis. 'S.E.' stands for 'single epoch'.

multi-epoch data structure (MEDS). Finally we come to the shape measurement process itself, which forms the bulk of this paper. We measure galaxy ellipticities with two quantities e_1 and e_2, and the ensemble shear in terms of either γ_1 and γ_2 or the reduced shears g_1 and g_2 (Bartelmann & Schneider 2001).

The difficulty of accurately recovering ellipticities and shears from noisy, pixelized data, as well as the value of exploring multiple approaches to it, was quickly recognized. In response, a series of shape measurement challenges have sought to compare and test the various codes available. The past decade has seen several such exercises, most notably the Shear Testing Programme and GRavitational lEnsing Accuracy Testing (GREAT) challenges (Heymans et al. 2006; Massey et al. 2007; Bridle et al. 2010; Kitching et al. 2012; Mandelbaum et al. 2015), which have illuminated many of the issues that the field must solve.

Galaxy shape measurement methods can be split into two broad categories. Each must correct for the imaging processes, such as PSF convolution, which alter the apparent shapes of galaxies. The first is forward-modelling methods, in which parametric models of galaxy images are generated, propagated through the observing processes, and compared to the data in order to obtain a likelihood or other goodness-of-fit metric for the galaxy parameters. The second class, inverse methods, measure second-order moments or other values

on the image data, then apply corrections to compensate for the effects of the observing process. Early methods like KSB (Kaiser, Squires & Broadhurst 1995) and Shapelets (Refregier 2003) largely fall into the latter category, but recent work has mostly focused on model-based methods.

Within each of these categories there are a great many methodologies and specific codes, each with different assumptions and designs, which lead to advantages and drawbacks in different domains. One advantage of model-fitting methods is that it is easier to enumerate the biases that can afflict them.[1]

We can characterize these biases with a Taylor expansion as (Heymans et al. 2006)

$$g_i = (1 + m_i)g_i^{\text{tr}} + c_i, \qquad (1)$$

where g_i is a shear estimate for the $i = (1, 2)$ component of shear and g_i^{tr} is the true value. The dominant contribution to the c_i term usually arises from the PSF ellipticity, so we sometimes re-write this as

$$g_i = (1 + m_i)g_i^{\text{tr}} + \alpha e_i^{\text{PSF}} + c_i \qquad (2)$$

for some α and the PSF ellipticity e^{PSF}. The three largest biases that generate various combinations of m, c, and α are usually model bias, noise bias, and selection bias.

Model bias, the mismatch between an assumed galaxy image model and the true one, was shown in the GREAT3 challenge to cause an error of up to ∼1 per cent, which is comparable to the target errors in the current generation of surveys (Mandelbaum et al. 2015).

Noise bias is often the dominant shear measurement bias, and is more properly understood as an estimator bias. It affects methods that use the maximum point in the likelihood of model parameters or similar quantities as a point-wise estimator of the ellipticity, since these quantities are inherently biased if the probability distributions are asymmetric (Bernstein & Jarvis 2002; Hirata & Seljak 2003; Kacprzak et al. 2012), as is almost always the case for shear estimation. It typically causes a ∼10 per cent bias if untreated. One solution is to account for the shape of the posterior surface; methods for doing this have been developed in Miller et al. (2007) and Bernstein & Armstrong (2014) and was used by the DES-SV analysis in the NGMIX code (Sheldon 2015).

Selection bias is the result of objects being included or excluded from the catalogue in a way that depends on their intrinsic shapes or the shear to which they are subject. Every catalogue has some selection function, and nearly all will result in biased shear estimates. Even if the measurements on individual galaxies are completely accurate (i.e. the histogram of their shapes can be recovered perfectly), if we preferentially select, for example, the roundest galaxies, we will systematically underestimate the cosmological shear. If noise bias is an estimator bias, then selection bias can be thought of as a *representativeness* bias. These effects have been found to be more pervasive than previously believed, and were found to cause 5 per cent biases in Jarvis et al. (2016). They make comparison between shear samples particularly difficult, and can arise from the detection process itself or from cuts or binning applied to measured results – the latter was found to be much more significant in Fenech Conti et al. (2017).

There are multiple practical paths to the elimination of these various shear estimation biases. The simplest is to accept their existence

and estimate the shear errors by processing simulated data with known input shear through the same pipeline as the real data. Early calibration methods using simulations used a single global calibration factor (Schrabback et al. 2007; Jee et al. 2013). More recent methods have derived a calibration value per-object as a function of measured galaxy properties, e.g. Jarvis et al. (2016), Hildebrandt et al. (2017). This is the approach taken by the IM3SHAPE code in this paper.

These calibration methods require simulations that are very carefully matched to the properties of the given data; otherwise the calibration factors used can be incorrect. Methods which do not depend on simulations can reduce the scale of this challenge, or avoid it completely. There has been a flurry of interest in recent years in the various ways one could do this. In Fenech Conti et al. (2017), the KiDS collaboration used *self-calibration*, in which a simulated version of each object is generated from the best-fitting model parameters and re-measured – this removes about half of the noise bias and reduces required simulation volumes. Huff & Mandelbaum (2017) and Sheldon & Huff (2017) describe the *metacalibration* method used by the METACALIBRATION pipeline in this paper, which calibrates the estimator biases by applying an added shear to the *real* galaxy images and gauging its effect on galaxy measurement and selection. This proves highly effective in tests on simulations. Another recent approach, the Bayesian Fourier Domain method (BFD; Bernstein & Armstrong 2014), uses deeper data to provide an implicit model, avoiding model bias, and prescribes a selection process for which biases are calculable from a full probabilistic treatment. BFD estimates will be investigated in future DES shear catalogues.

The DES shape measurement methodology in the DES-SV period was exhaustively detailed in Jarvis et al. (2016), hereafter J16. Many aspects of our methodology are the same as in SV, so this paper builds on that work – unchanged aspects of the process that are not explained here are detailed there.

This paper is organized as follows: in Section 2 we describe the observations analysed in this work. In Section 3 we describe the measurement of the PSF. Sections 4 and 5 describe the construction of our two catalogues, METACALIBRATION and IM3SHAPE, respectively, including the calibration simulations used in the latter. Section 6 describes a series of tests validating that the catalogues have sufficient accuracy for cosmic shear, cross correlations, and other measurements of the lensing signal. Section 7 discusses procedures for use of the catalogues, including appropriate systematic error priors and the correct use of the calibration systems. We conclude in Section 8.

2 DATA

2.1 Observing period and conditions

The Dark Energy Survey (DES) Year One (Y1) catalogues described here are based on observations taken using the Dark Energy Camera (DECam, Flaugher et al. 2015) on the Blanco telescope at the Cerro Tololo Inter-American Observatory during the first full season of DES operations. Y1 images were acquired between 2013 August 31 and 2014 February 9 (Diehl et al. 2014). The nominal plan for the DES Wide Survey is to image the entire 5000 deg^2 footprint 10 times in each of the g, r, i, z, and Y filters over five seasons of operation. DECam images have an average pixel scale of 0.263 arcsec. In Y1 we opted to target only the regions overlapping the South Pole Telescope (SPT) survey footprint at $-60° \lesssim \delta \lesssim -40°$ and the equatorial SDSS 'Stripe 82' region covering $-1.26° < \delta <$

---

[1]Problems analogous to these issues affect model-independent methods too, but it is typically harder to interpret their impact.
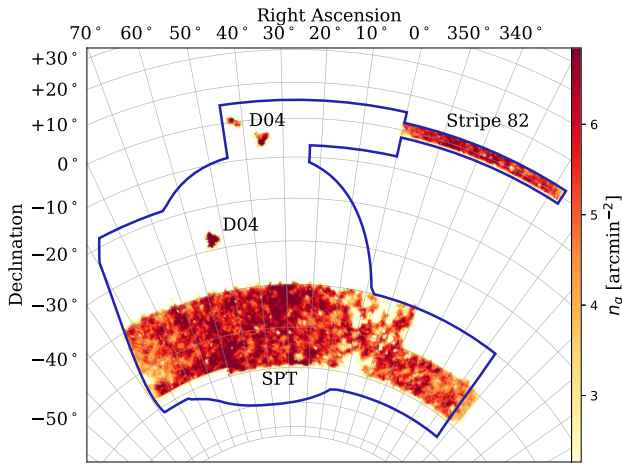
Figure 2. The DES Y1 shear catalogue footprint with galaxy density of the METACALIBRATION catalogue shown with the nominal 5-yr DES footprint outline overlayed. IM3SHAPEis qualitatively similar, but slightly shallower. We define three fields: (1) The large, southern field overlapping with SPT, which has been selected for DES Y1 science applications due to contiguity. (2) The long equatorial strip overlapping with SDSS Stripe 82. (3) The disjoint supernovae and spectroscopic-overlap fields, which have been selected from the four exposure depth (D04) GOLD catalogue. Additional D04 fields far from the SPT region are not shown. The densities are not corrected for the detection fraction within each pixel. The Albers equal-area projection is used.

$+1.26°$ and $20{:}00h < \mathrm{RA} < 04{:}00h$, comprising about 30 per cent of the full footprint. The goal was to obtain four 'tilings' per filter over this region in Y1, rather than cover the full footprint with two tilings, because four-tiling coverage is much more robust to cosmic rays and per-exposure systematic errors, especially after considering the gaps in the functional imaging area of DECam. Given these factors, a two-tiling coverage would not have led to a viable shape catalogue. The vagaries of the weather led to non-uniform coverage of the Y1 target area. Fig. 2 shows the footprint of the Y1 METACALIBRATION shape catalogue after the cuts described below for minimum depth in each filter.

In comparison to the SV catalogues described by J16, the main areas of the Y1 shape catalogues cover a much larger area (1500 deg² versus 140 deg²) but with a lower integrated exposure time (up to 4×90 s exposures per filter in *griz* versus 10×90 s nominal in SV). The quality of the Y1 imaging is superior to that taken in SV in several respects:

(i) The telescope tracking servos exhibited oscillations in right ascension during most of the SV period, leading to more elliptical and less stable PSFs. This was fully remedied for Y1.

(ii) More rigorous assessment of image quality was in place for Y1, and exposures failing to meet certain thresholds for seeing, cloud extinction, and sky brightness were rejected after each night's observing and placed back onto the observing queue (Neilsen et al. 2016).

(iii) The feedback system using out-of-focus stellar images to maintain focus and alignment of the camera (Roodman, Reil & Davis 2014) was improved substantially by the start of Y1, further stabilizing the PSF quality.

(iv) Thermal control of the Blanco mirror and dome was improved between the SV and Y1 periods.

(v) Improved baffling of the filters reduced the incidence of stray-light contamination, and improvements in software identification of

image artefacts also reduced the number of spurious features in the images.

(vi) The SV observing sequences concentrated most of the observations of a given part of the sky into a small number of nights. By Y1 we had adopted a wide-survey scheduler which penalizes repeat coverage in a given filter on a given night. This decorrelates weather variation from the sky coordinates and leads to more uniform survey quality.

(vii) The shutter-closed time between exposures was reduced, increasing the observing efficiency ~2.5 per cent.

One degradation in camera performance during Y1 is that one of the 62 CCDs in the DECam science array failed on 2013 November 30. Most of the Y1 data therefore has one less usable CCD's worth of data per exposure.

2.2 Object catalogue

The initial selection of galaxies on which shape measurement was performed is detailed in Drlica-Wagner et al. (2018), and the selection described therein is denoted the GOLD catalogue. The image reduction, photometric calibration, and detection from coadded images to the catalogues are described in that paper, and the star–galaxy separation described therein is applied to the IM3SHAPE catalogue. The full region the catalogue covers is shown in Fig. 2, though our cosmological analyses will use only the southern region that overlaps with the SPT survey.

2.3 Galaxy selection

Galaxies are distinguished from stars in GOLD using a classifier called MODEST, which is based on the SEXTRACTOR SPREAD_MODEL variable (Bertin & Arnouts 1996; Soumagnac et al. 2015), which discriminates between objects best fit as a point source versus an extended object. In this paper the IM3SHAPE selection cuts made use of MODEST, in the high-purity variant described in Drlica-Wagner et al. (2018). The METACALIBRATION catalogue and the PSF star selection used alternative criteria. The overall magnitude distributions of the selections, and of the final shape catalogues, are shown in Fig. 3.

Images within 30 pixels of the edge of a CCD are removed from the selection because of a 'glowing-edge' effect which gives pixels there a different effective size (Plazas, Bernstein & Sheldon 2014b).

2.4 Astrometry

The DES Y1 single-epoch pipeline derives an astrometric solution for each exposure by comparing object positions across the focal plane to the reference catalogue UCAC-4 (Zacharias et al. 2013) using the AstrOmatic utility SCAMP (Bertin 2006, 2010). These solutions typically have 200–300 mas RMS in their residuals with respect to the reference catalogue. In order to produce high-quality co-added images in the multi-epoch pipeline, an astrometric refinement step is used prior to combining the images. That step considers catalogued objects with S/N > 10 from all exposures (at all bands) that overlap the coadd tile. A simultaneous astrometric fit is made, again using SCAMP but now using the 2MASS Point Source Catalogue as an astrometric reference (Skrutskie et al. 2006). The refined astrometric solutions are used to update the world coordinate system (WCS) for each image prior to coaddition. The resulting fits typically have an internal astrometric residual of 25–35 mas (RMS)
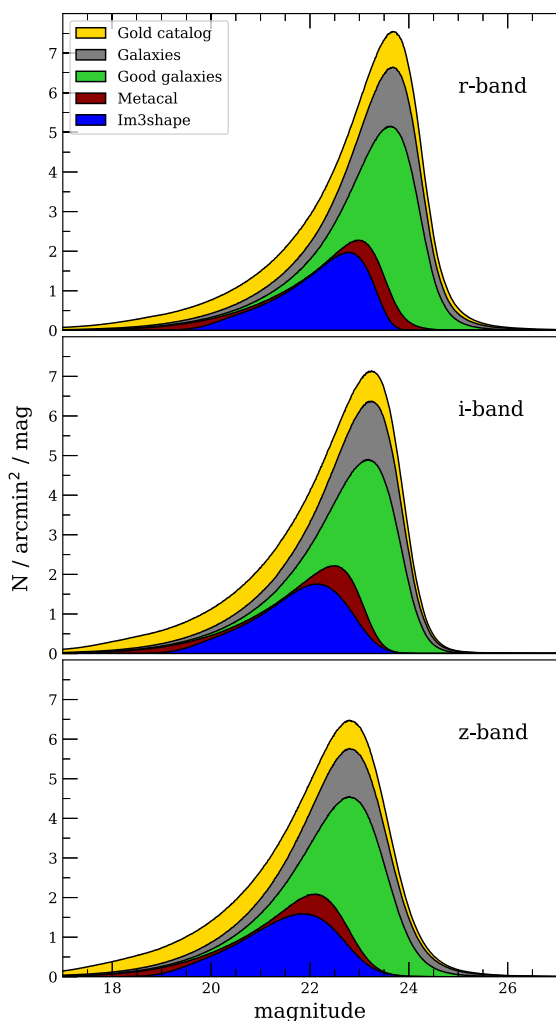
Figure 3. Magnitude histograms showing different selections of the DES Y1 catalogues. Values are measured with the multi-object fitting (MOF) method described in Drlica-Wagner et al. (2018). The GOLD catalogue is the input detection catalogue described in Section 2.2. 'Galaxies' are those identified as galaxies by the process described in Section 2.3. 'Good' galaxies are those with no indication of blending or extreme colours from SEXTRACTOR. The METACALIBRATION and IM3SHAPE histograms show objects in the final shape catalogues, after method-specific cuts.

between the individual images/exposures and an external astrometric residual of 250 mas with respect to the 2MASS catalogue.

2.5 COSMOS data

For several simulations and validation tests we make use of a galaxy catalogue from Advanced Camera for Surveys (ACS) imaging of *HST*'s COSMOS field (Koekemoer et al. 2007; Scoville et al. 2007). The catalogue of ∼73 000 objects has been 'whitened' (correlated noise removal; see Rowe et al. 2015), and is a deeper superset of the galaxies used in the GREAT3 challenge.[2] It extends significantly beyond the Y1 detection limit of $M_{\rm r,lim} = 23.4$ (Drlica-Wagner et al. 2018), reaching ∼25.2 mag in the *HST F*814*W* filter and ∼27.9 mag in the DES *r* band.

[2]http://great3.jb.man.ac.uk/

2.6 Blinding

The DES Y1 shear catalogues were blinded to mitigate experimenter bias, in which analysis methodology may be intentionally or otherwise tuned so that results match expectations. The blinded catalogues have all ellipticities *e* as defined below in equation (4) transformed via $|\eta| \equiv 2 \operatorname{arctanh} |e| \to f |\eta|$, with a hidden value 0.9 < *f* < 1.1. This mapping preserves the confinement of the *e* values to the unit disc while rescaling all inferred shears. DES cosmological analyses making use of these catalogues finalized their analysis methodology before being supplied with the unblinded catalogues. Cosmological parameter estimation for these projects incorporate further secondary blinding strategies as described in their respective papers.

In the interests of full disclosure we must report that two independent but equivalent errors in the two shape pipelines meant that the multiplicative calibration process was incorrectly applied after the blinding process instead of before, partially undoing its effects. The transformation described above is not a purely multiplicative one, since it acts on arctanh |*e*| instead of *e*, but for small ellipticities it is nearly so. Since the calibration removed a multiplicative bias, This meant that most of the effect of blinding was undone by the calibration process. Since the mistakes were equivalent, the two catalogues remained consistent after blinding, and no errors were caused in any tests or comparisons.

This fact was discovered during the cosmological analysis, but after the catalogues had been frozen and the tests presented in this paper finalized. The error was not disclosed to the full analysis team, so most members remained effectively blinded. Additionally, the individual cosmology analyses in Troxel et al. (2017) and DES Collaboration (2017) included another layer of blinding: all cosmology constraint plots included shifts in the positions of the DES results, so that the absolute position could not be compared to existing results or preconceived expectations. While these errors could not therefore have resulted in any experimenter bias being possible, they will be corrected in the next DES analysis.

3 PSF ESTIMATION

One of the most important aspects of image characterization is accurately estimating the PSF. The PSF describes how a point source of light in the sky is mapped into a two-dimensional profile on the image. The images of galaxies are the convolution of the true surface brightness profile with the PSF.

Since stars are essentially point sources, observations of stars give us a direct (albeit noisy) estimate of the PSF at the locations of the stars. However, the PSF is not constant across the field of view, so the PSF must be interpolated from the locations of stars, where it is observed, to the locations of galaxies, where it is needed.

The process for PSF estimation in Y1 is largely unchanged from the procedure used in J16. We briefly recap the procedure described therein, emphasizing the changes we have made since SV.

3.1 Selection of PSF stars

We use the same method for identifying and selecting PSF stars as J16. The initial identification of candidate PSF stars involved using a size–magnitude diagram of all the objects detected on the image. For the magnitude, we used the SEXTRACTOR measurement MAG_AUTO. For the size, we use the scale size, σ, of the best-fitting elliptical Gaussian profile using the adaptive moments algorithm HSM (Mandelbaum et al. 2005).
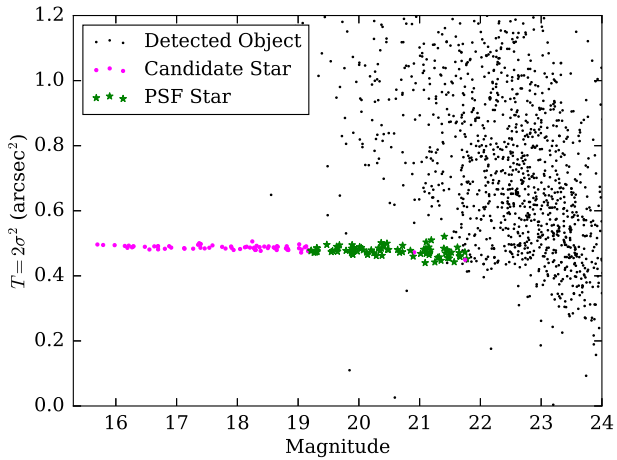
Figure 4. An example size–magnitude diagram for a single CCD image, used to identify stars.

The stars are easily identified at bright magnitudes as a locus of points with size nearly independent of magnitude. The galaxies have a range of sizes, all larger than the PSF size. The candidate PSF stars are taken to be this locus of objects from about $m \approx 15$, where the objects begin to saturate, down to $m \approx 22$, where the stellar locus merges with the locus of faint, small galaxies.

From this list of candidate stars, we remove objects that are not suitable to use as models of the PSF. Most importantly, we remove all objects within 3 mag of the faintest saturated star in the same CCD exposure in order to avoid stars whose profiles are affected by the so-called 'brighter-fatter effect' (Antilogus et al. 2014; Gruen et al. 2015; Guyonnet et al. 2015) – see Section 3.2. This magnitude cut-off varies between 18 and 19.5.

In addition, we remove stars that overlap the 'tape bumps'. The CCDs on DECam each have six spots where 2 mm × 2 mm ×100 μm-thick spacers were placed behind the CCDs when they were glued to their carriers (see Flaugher et al. 2015). This alters the electric field and hence the PSF is distorted near each spacer. Fig. 4 shows such a size–magnitude diagram for a representative CCD image. The stellar locus is easily identified by eye, and the stellar sample identified by our algorithm is marked in pink and green. The pink points are stars that are removed by our various selection cuts, while the green points are the stars that survive these cuts.

We find a median of 115 useful stars per CCD image, which we use to constrain the PSF model. The distribution of PSF stars per CCD exposure is shown in Fig. 5. In Fig. 6, we show the distribution of the median measured full-width half-maximum (FWHM) for the PSF stars used in our study, restricted to the exposures used for shear measurements. The overall median seeing is 0.96 arcsec, which is significantly better than we obtained in the SV observations (108), but still somewhat larger than the original target of 0.90 arcsec.

Occasionally, this process for selecting stars fails, in which case we add the CCD's image to a 'blacklist' of those not used for shear estimation. For instance, if fewer than 20 stars are identified as PSF stars (e.g. because there is a very bright star or galaxy dominating a large fraction of the CCD area), then we blacklist the CCD image. Sometimes the star-finding algorithm finds the wrong stellar locus and ends up with far too many 'stars' or finds a very large FWHM (>3.6). These CCDs are similarly excluded from consideration. These PSF blacklist entries are added to the GOLD-catalogue blacklist, which includes CCDs with large ghosts,
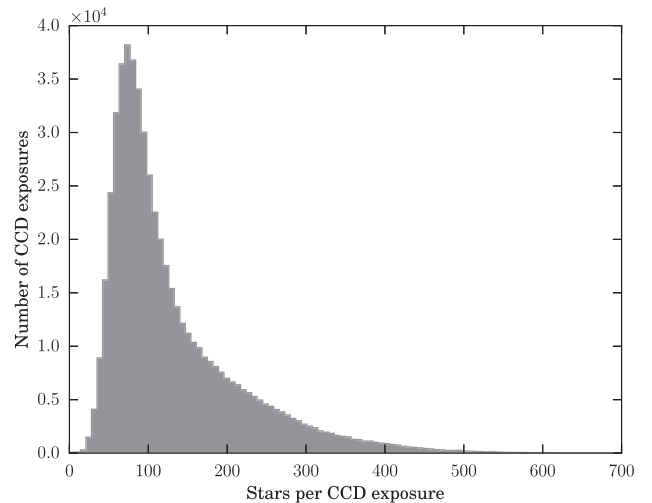
Figure 5. The distribution of the numbers of stars used to constrain the PSF model per CCD image.
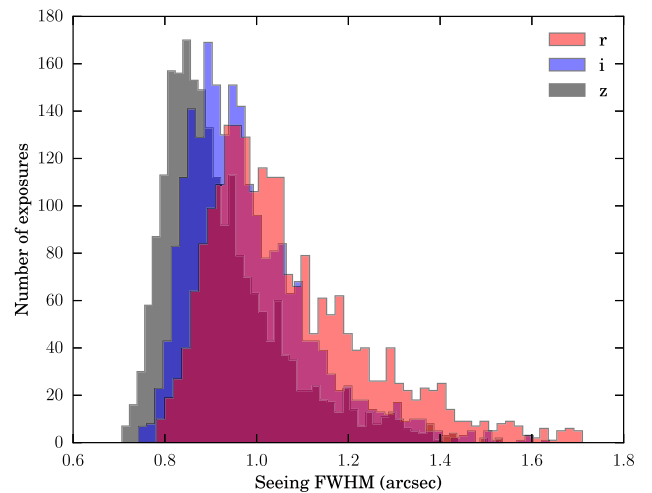
Figure 6. The distribution of the median seeing FWHM of the stars used to model the PSF in the *riz* bands. The median seeing of these distributions is 1.03 in the *r* band, 0.95 in the *i* band , 0.89 in the *z* band, and 0.96 in the three bands overall.

scattered light, satellite trails, or other apparent defects (Drlica-Wagner et al. 2018).

3.2 PSF measurement and interpolation

We used the software package PSFEX (Bertin 2011) to measure the surface brightness profile $I(x, y)$ of the PSF stars selected above as well as to interpolate between the locations of the stars. We used the following configuration parameters for PSFEX:

```
BASIS_TYPE PIXEL
PSF_SAMPLING 0.5
PSF_SIZE 101,101
PSFVAR_KEYS XWIN_IMAGE,YWIN_IMAGE
PSFVAR_GROUPS 1,1
PSFVAR_DEGREES 2
```

The one change from the procedure described in J16 is to switch the BASIS_TYPE from PIXEL_AUTO to PIXEL. With
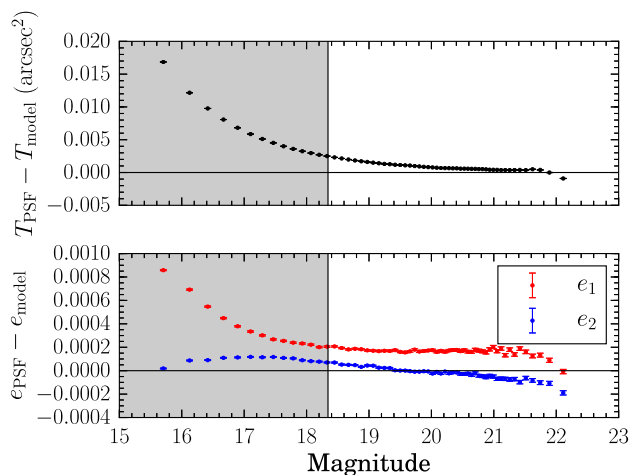
Figure 7. The relative model size (top) and shape (bottom) residual of stars. To reduce the impact of the brighter-fatter effect bright stars are excluded from our PSF models; the cut-off varies between CCD exposures but the shaded region shows a typical example.

PIXEL_AUTO, there was an overall mean residual in the size of the PSF models compared to the measured sizes of the stars. Switching to PIXEL yields near-zero size residual for faint stars (i.e. those unaffected by the brighter-fatter effect).

In Fig. 7 we show size and shape residuals of all identified stars, relative to our standard PSFEX model, which uses only the faint ones. The sizes and shapes are defined in terms of the second moments of the surface brightness profile (Seitz & Schneider 1997):

$$T = I_{xx} + I_{yy} \tag{3}$$

$$e = e_1 + ie_2 = \frac{I_{xx} - I_{yy} + 2iI_{xy}}{I_{xx} + I_{yy} + 2\sqrt{I_{xx}I_{yy} - I_{xy}^2}}, \tag{4}$$

where the moments are defined as

$$I_{\mu\nu} = \frac{\int dx\, dy\, I(x, y)(\mu - \bar{\mu})(\nu - \bar{\nu})}{\int dx\, dy\, I(x, y)}. \tag{5}$$

The moments are measured using HSM (Mandelbaum et al. 2005). The quantity T is one measurement of the square of the object radius.

The brighter-fatter effect is seen at bright magnitudes to lead to biases in both the size and shape (especially e_1). This motivates the cut described above in Section 3.1 and shown in the shaded region. There is a small residual error in e_1 even at the faintest magnitudes, and we are unable to find settings to PSFEX that eliminate this bias. However, the size residual is now seen to be consistent with zero at faint magnitudes, which was not the case for the SV analysis.

In Fig. 8, we show both the raw PSF shape and the residuals as a function of position on the focal plane. The residuals are small, but not quite zero, and there is an evident rippling pattern. The impact of these spatially correlated residuals is investigated below in Section 3.3.

3.3 PSF model diagnostics

The errors in the PSF model seen in Fig. 8 will propagate into the galaxy shapes and inferred lensing shear. To estimate the impact of PSF modelling errors on the shear two-point correlation function,

ξ_+ we turn to the ρ statistics (Rowe 2010; Jarvis et al. 2016):

$$\rho_1(\theta) \equiv \left\langle \delta e_{\rm PSF}^*(\boldsymbol{x}) \delta e_{\rm PSF}(\boldsymbol{x} + \boldsymbol{\theta}) \right\rangle \tag{6}$$

$$\rho_2(\theta) \equiv \left\langle e_{\rm PSF}^*(\boldsymbol{x}) \delta e_{\rm PSF}(\boldsymbol{x} + \boldsymbol{\theta}) \right\rangle \tag{7}$$

$$\rho_3(\theta) \equiv \left\langle \left(e_{\rm PSF}^* \frac{\delta T_{\rm PSF}}{T_{\rm PSF}} \right)(\boldsymbol{x}) \left(e_{\rm PSF} \frac{\delta T_{\rm PSF}}{T_{\rm PSF}} \right)(\boldsymbol{x} + \boldsymbol{\theta}) \right\rangle \tag{8}$$

$$\rho_4(\theta) \equiv \left\langle \delta e_{\rm PSF}^*(\boldsymbol{x}) \left(e_{\rm PSF} \frac{\delta T_{\rm PSF}}{T_{\rm PSF}} \right)(\boldsymbol{x} + \boldsymbol{\theta}) \right\rangle \tag{9}$$

$$\rho_5(\theta) \equiv \left\langle e_{\rm PSF}^*(\boldsymbol{x}) \left(e_{\rm PSF} \frac{\delta T_{\rm PSF}}{T_{\rm PSF}} \right)(\boldsymbol{x} + \boldsymbol{\theta}) \right\rangle, \tag{10}$$

where $e_{\rm PSF}$ and $\delta e_{\rm PSF} \equiv e_{\rm PSF} - e_{\rm model}$ are the measured ellipticity of the PSF model at the locations of stars and its measured residual, respectively; $T_{\rm PSF}$ and $\delta T_{\rm PSF} \equiv T_{\rm PSF} - T_{\rm model}$ are the size of the model and its residual; the asterisk denotes complex conjugation; and the averages are taken over pairs of stars separated by angle $\boldsymbol{\theta}$. These statistics neglect anisotropy in PSF errors, but will indicate the first-order effects on the correlation functions. There is no equivalent effect on ξ_-, where such additive effects are negligible.

The values $\delta T_{\rm PSF}/T_{\rm PSF}$ as measured from sizes of reserved stars are typically positive, meaning stars are slightly larger than smooth polynomial PSF models predict. In DES data we find mean size errors from this effect $\langle \delta T_{\rm PSF}/T_{\rm PSF} \rangle \sim 8.3 \times 10^{-4}$ and a much larger size variance: $\langle (\delta T_{\rm PSF}/T_{\rm PSF})^2 \rangle^{1/2} \sim 3 \times 10^{-2}$.

For these tests, we constructed PSF models using only 80 per cent of the PSF stars that were selected as described in Section 3.1. The PSF model was then interpolated to the locations of the other 20 per cent of the stars that had been reserved from the modelling step. This is an improvement over the procedure used by J16 where the same stars that were used for making the PSF model were used in the ρ statistics. The statistics are shown, binned by $|\boldsymbol{\theta}|$, in Fig. 9 averaged over single-epoch stellar observations in r, i, and z bands. The averages thus include pairs of observations from different exposures as well as those from the same exposure, thus corresponding to the way these residuals impact the two-point shear correlation of the shear estimates of the galaxies.

The ρ statistics for individual exposures in Y1 are similar to those obtained for SV in J16. The SV data, however, have a mean of 19.7 usable exposures per galaxy in the *riz* bands, while the Y1 data presented here have a mean of only 8.4 exposures. When the modelling errors are uncorrelated between exposures for a given star or galaxy target, the survey-averaged statistics scale as $\rho \propto 1/N_{\rm exposures}$. As such, the amplitude of the ρ_1 statistic is significantly larger for Y1 than reported for SV in J16. In addition, the fact that we are using reserved stars this time also increased the measured correlations somewhat compared to SV, especially at large scales. In the SV statistics the mean residual was close to zero by construction, so the statistics were probably spuriously low. The mean residual of the reserved stars is expected to be a better estimate of the actual error in the fitted PSF models.

The PSF modelling residuals constitute the largest known additive systematic error on the estimated shear values. For two-point shear statistics such as ξ_+, we expect the additive error due to these statistics to be (J16, equation 3.17):

$$\delta\xi_+(\theta) = \left\langle \frac{T_{\rm PSF}}{T_{\rm gal}} \right\rangle^2 (\rho_1(\theta) + \rho_3(\theta) + \rho_4(\theta))$$
$$- \alpha \left\langle \frac{T_{\rm PSF}}{T_{\rm gal}} \right\rangle (\rho_2(\theta) + \rho_5(\theta)), \tag{11}$$

where α is the amount of 'leakage' of the PSF shape into the galaxy shape (see Section 6.2.2). We discuss the impact of this contribution
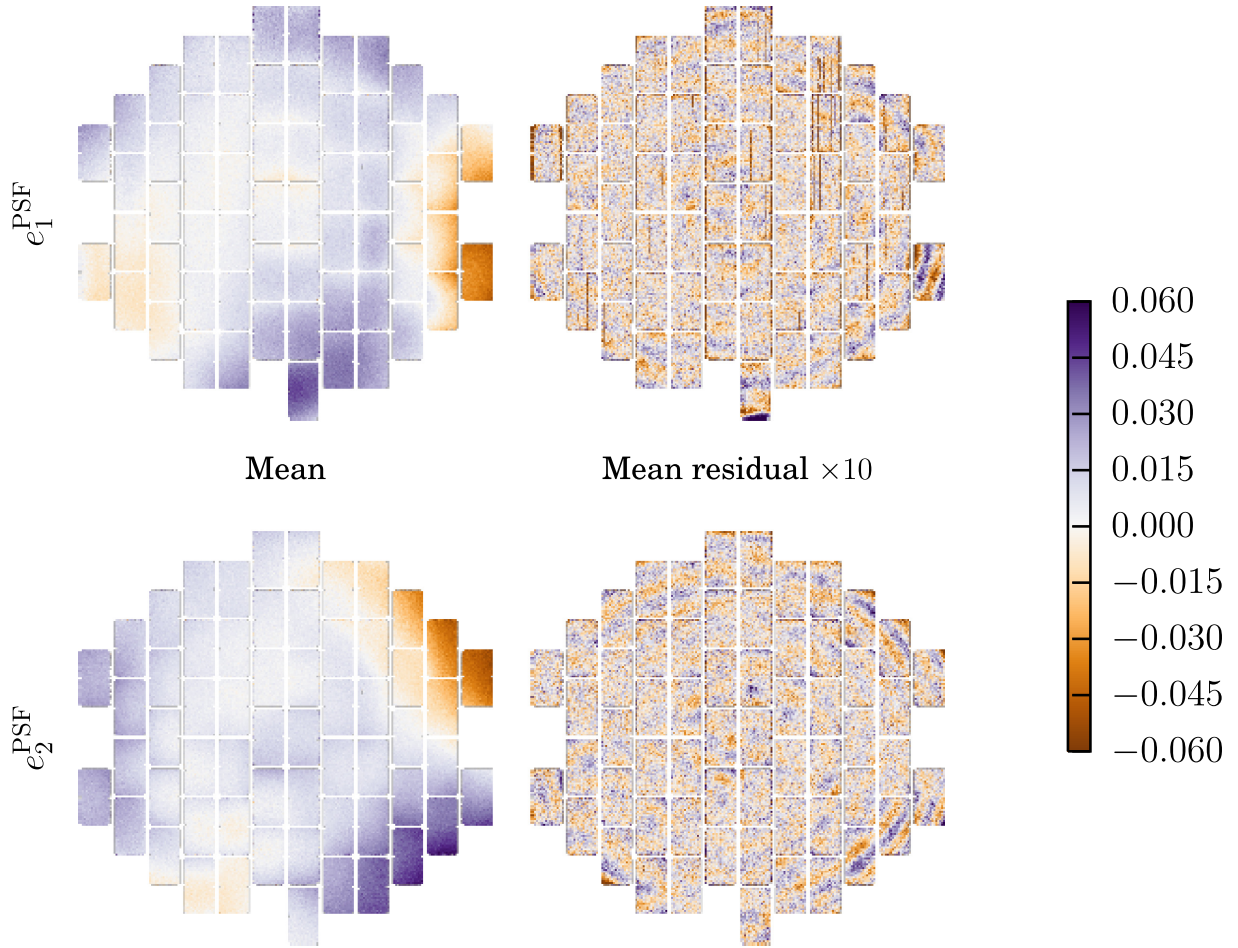
Figure 8. The mean PSF ellipticity (left) and mean residual after subtracting the PSFEX model ellipticity (right), binned by position in the focal plane. The residual is multiplied by a factor of 10 to be visible in the same colour scale.
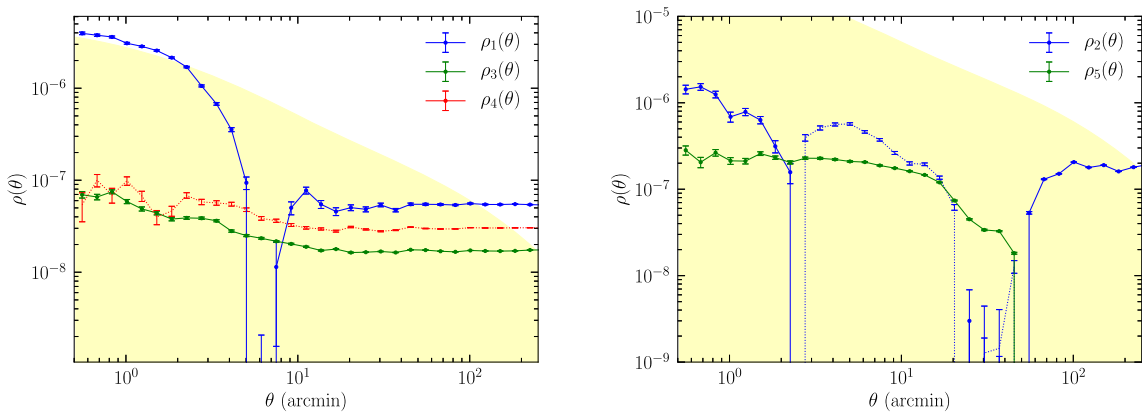
Figure 9. The ρ statistics for the PSF shape residuals. Negative values are shown in absolute value as dotted lines. Requirements on the ρ statistics are specific to individual science cases; the yellow fill is a general guide, rather than a requirement, and is 10 per cent of the value of the weakest cosmic shear ξ_+ signal, which is from the lowest redshift tomographic bin (for this bin only scales above $\theta \approx 7$ arcmin were used in the analyses in Troxel et al. 2017 and DES Collaboration 2017). It pessimistically assumes $\alpha = 0.1$ and $T_{\mathrm{PSF}}/T_{\mathrm{gal}} = 1$. Contributions to the signal from the flat regimes at large scales will be absorbed by the marginalization over the mean shear discussed in Section 7.1.

to ξ_+ further in Troxel et al. (2017). For other analyses of these data that are sensitive to additive errors, we also recommend explicitly accounting for the potential impact of additive systematics due to the PSF model residual.

4 THE METACALIBRATION CATALOGUE

4.1 METACALIBRATION overview

Our primary catalogue uses *metacalibration*, a new method for shear measurement that derives shear calibrations directly from the available imaging data. Metacalibration is described in detail in Huff & Mandelbaum (2017) and Sheldon & Huff (2017), hereafter SH17.

The principle behind METACALIBRATION is to measure the response of a shear estimator e to shear. Unlike in most methods this response is not estimated from a suite of simulated images, but rather calculated directly for each observed image, using the scheme described below.

Any estimator that has sensitivity to shear can be used with metacalibration, and here we use measurements of galaxy ellipticity. For small shears, ellipticity estimators can be written as a Taylor expansion:

$$e = e|_{\gamma=0} + \left.\frac{\partial e}{\partial \gamma}\right|_{\gamma=0} \gamma + ...$$
$$\equiv e|_{\gamma=0} + R_\gamma \gamma + ..., \tag{12}$$

where we have defined the shear response matrix R_γ. The shear response is calculated by artificially shearing the images and remeasuring the ellipticity. We do this by directly deconvolving the PSF [by dividing the Discrete Fourier Transform (DFT) of the image by the DFT of the PSF image], applying a shear, and then reconvolving by a symmetrized version of the PSF (the latter steps using the GALSIM package, Rowe et al. 2015). We then form a numerical derivative: for a given element of the response matrix, we calculate

$$R_{\gamma\,i,j} = \frac{e_i^+ - e_i^-}{\Delta\gamma_j}, \tag{13}$$

where e_i^+ is the measurement of component i made on an image sheared by $+\gamma_j$, e_i^- is the measurement made on an image sheared by $-\gamma_j$, and $\Delta\gamma_j = 2\gamma_j$. We used an applied shear $\gamma_j = 0.01$.

When measuring a shear statistic, such as mean shear or a shear two-point function, these responses can be averaged appropriately to produce a calibrated result. For the example of mean shear, we can take the expectation value of equation (12). Keeping terms to first order in the shear, and assuming the mean ellipticity is zero in the absence of shear, we find

$$\langle e \rangle = \langle e \rangle|_{\gamma=0} + \langle R_\gamma \gamma \rangle \approx \langle R_\gamma \gamma \rangle, \tag{14}$$

With estimates of R_γ for each galaxy, we can form a weighted average:

$$\langle \gamma \rangle_w \approx \langle R_\gamma \rangle^{-1} \langle R_\gamma \gamma \rangle \approx \langle R_\gamma \rangle^{-1} \langle e \rangle, \tag{15}$$

where the subscript w implies this is a weighted average over the true shears. The generic correction for two-point functions was also derived in SH17 as

$$\xi = (\langle R^\alpha \rangle \langle R^\beta \rangle)^{-1} \langle e^\alpha e^\beta \rangle \tag{16}$$

for two samples of objects (e.g. tomographic bins) α and β where $\langle e^\alpha e^\beta \rangle$ is a standard two-point correlation function estimate. The

application of this method to other specific statistics should be worked out carefully, as the details of the averaging are important.

We can also correct for selection effects, for example shear biases that may occur when placing a cut on signal-to-noise ratio S/N. This is accomplished by measuring the mean response of the estimator to the selection, repeating the selections on quantities measured on sheared images. Again taking the example of mean shear, a given element of the mean selection response matrix $\langle R_S \rangle$ is

$$\langle R_S \rangle_{i,j} \approx \frac{\langle e_i \rangle^{S+} - \langle e_i \rangle^{S-}}{\Delta\gamma_j}, \tag{17}$$

where $\langle e \rangle^{S+}$ and $\langle e \rangle^{S-}$ represent the means of ellipticities measured on images without artificial shearing, but with selection based on parameters from positively and negatively sheared images, respectively. The full response for the mean shear is then given by the sum of the shear response and selection response

$$\langle R \rangle = \langle R_\gamma \rangle + \langle R_S \rangle. \tag{18}$$

For the ellipticity estimators used here we have found that the response matrix R is on average diagonal, and that $R_{11} \approx R_{22}$, so that a single scalar value characterizes the response.

METACALIBRATION was tested using an extensive set of simulations, and proved to be unbiased for galaxy images with realistic properties matching the deep COSMOS data, and noise and PSFs similar to DES data (SH17). Furthermore, METACALIBRATION was shown to be robust to the presence of stars in the sample if the PSF is well determined. There are additional challenges for real data, which we will discuss below.

4.2 METACALIBRATION in DES Y1

For DES we ran METACALIBRATION in a mode similar to that used in SH17, using the METACALIBRATION implementation available in the NGMIX software package[3] (Sheldon 2015). We used an estimate of each object's ellipticity as the basis for shear estimation, to be calibrated using METACALIBRATION. The total time for a run of METACALIBRATION on DES Y1 data was about 150 000 CPU hours for the full set of 139M detected objects. The calculations were performed using computational resources at the SLAC National Accelerator Laboratory.

To determine the ellipticity, we fit the images associated with each object to a simple parametric model using the NGMIX code. For efficiency reasons, we chose a single Gaussian to model the object, convolved by a model of the PSF. As described above, we model the PSF in each image using the PSFEX code. We then reconstructed an image of the PSF at the location of each object from PSFEX output using a separate package.[4]

This full PSF image was used for the devonvolution step in the metacalibration process. For the shape fitting stage itself we represented the PSF as a single Gaussian, for efficiency reasons. A Gaussian is not a good description of the DES PSF, but SH17 find that this does not limit our ability to calibrate the shear estimate, because the response accounts for any mismatch between the actual PSF and the model used for fitting.

The full model for each galaxy image was the analytic convolution of the object Gaussian with the Gaussian representation of the

---

[3]The NGMIX package is freely available at https://github.com/esheldon/ngmix.
[4]https://github.com/esheldon/psfex

PSF. We then found the parameters that maximized the likelihood, as calculated across all available imaging epochs and bands r, i, z.

We simultaneously fit images from all available observing epochs, and all available band passes, with a free flux in each band. In general the r band is the most powerful band and gives the most shape signal, though the others do add significant information. The total Gaussian model has five structural parameters, shared between all band passes, plus a free flux for each band pass. The structural parameters are two for the centre in sky coordinates, two for ellipticity components, and one for the size T as in equation (3) (equal to the trace of the Gaussian's covariance matrix). These quantities were measured for the unsheared as well as artificially sheared images discussed in Section 4.

We applied priors on all model parameters. These priors were uninformative, except for the prior on ellipticity, which we found necessary to provide a stable fit for faint objects: we used the isotropic unlensed distribution presented in (Bernstein & Armstrong 2014, equation 24), with $\sigma = 0.3$. The details of this prior are not important, because METACALIBRATION can accurately calibrate this shear estimator as long as the fitting is stable (SH17).

Real data present significant challenges that were not tested in the simulations of SH17. For this work we tested the following additional issues:

(i) Shear estimation using multi-epoch data.
(ii) Effects of neighbouring objects.
(iii) PSF modelling and interpolation errors.

We show tests using simulations for (i) in Section 4.3, for (ii) in Section 4.4, and for (iii) in Section 4.5. We also show tests of (ii) using real data in Section 7.6.1. The behaviours of the response functions $R\gamma$ and R_s are described in Appendix F.

4.3 METACALIBRATION and multi-epoch data

METACALIBRATION was tested in SH17 in the simple case where each object is observed once. However, in DES we simultaneously fit to images from multiple observing epochs in each of multiple bands. Each object was thus imaged in different seeing and noise conditions, and was observed at different locations within the focal plane. Furthermore, galaxies do not in general have the same morphology in every band.

We generated simulations to mimic this scenario using the GAL-SIM simulation package (Rowe et al. 2015). For each object we generated a set of 10 images with different PSF, noise, and position offset within the image. The PSF size was drawn from a distribution similar to DES data, with mean FWHM = 0.9 arcsec (see Fig. 6). The PSF ellipticity was drawn from a truncated Gaussian with centre (0.0, 0.01) and width (0.01, 0.01). The noise was varied by 10 per cent, and the object was offset randomly within a pixel.

The galaxy morphology was chosen to be the model used in SH17: a combination of exponential disc and de Vaucouleurs bulge profiles, with additional simulated knots of star formation. Size and flux distributions were matched to the 25.2 mag limited sample from COSMOS. The fraction of light in the disc was chosen uniformly from 0 to 1, and the fraction of disc light in knots was also chosen uniformly from 0 to 1. To simulate morphological differences between bands we varied the flux and size of the object in each image by 10 per cent, and assigned a random ellipticity. The noise was chosen such that the minimum S/N for the sample was approximately 5 in the combined set of 10 images. The S/N definition was that used in GALSIM, which is the same definition used in the

GREAT3 simulations (Mandelbaum et al. 2015, equation 16). We applied a constant shear to each image of (0.02, 0.00).

We fit the images using the same code used for fitting DES data. We applied a selection similar to that in our data: S/N > 10 and size $T/T_{PSF} > 0.5$, where T_{PSF} is the size of the PSF determined from a Gaussian fit. We found no multiplicative bias m or additive bias c, with limits $m < 1 \times 10^{-3}$ (95 per cent) and $c < 2 \times 10^{-5}$ (95 per cent). We also applied various threshold and range cuts in S/N, flux, and size and again found no bias.

4.4 METACALIBRATION and blending

In this section we explore the effect of blending on METACALIBRATION shear estimation.

In principle, METACALIBRATION will correctly infer the shear applied even to complex blends of multiple objects. However, even if the calculated shear response is accurate, there will be uncertainty in the *interpretation* of the inferred shear for overlapping objects. Consider first a scenario where two overlapping objects are at the same redshift. The same lensing shear has been applied to both, as well as to the apparent separation of the pair, so the entire scene has been transformed with a single shear and the METACALIBRATION shear inference should be an unbiased estimate of this shear as long as the model fitting process is stable.

Now consider the case that the two objects are at very different redshifts. In this case, the two sources have been sheared by different amounts, and the separation between the pair depends on the different deflections applied to the light from each object. To facilitate a correct interpretation, a detection algorithm must determine that there are two objects present, and a deblending algorithm must accurately assign a fraction of the light in each pixel to each of the blended objects. Then the response must be measured separately for each object based on this flux assignment.

This flux assignment can in principle be done given some a priori assumptions on the morphology allowed for each galaxy, but can be exceedingly difficult when galaxies are highly irregular or heavily overlapped. In addition, the response of the deblending algorithm to shear can cause selection effects that may be significant.

In DES we have utilized two different approaches to dealing with blends. The first, and simplest, is the überseg algorithm (J16), which masks pixels close to neighbours rather than assigning a fraction of the light in each pixel to them.

We have also developed a second algorithm, called multi-object fitting (MOF, Drlica-Wagner et al. 2018), which does attempt to assign a fraction of the light in each pixel to sets of blended objects. In brief, MOF finds groups of overlapping galaxies using a friends-of-friends algorithm. Within a group, MOF sequentially applies forward-modelling of simple bulge/disc models to each source, subtracting the models for all other sources in the group. MOF fits use all available imaging data in the g, r, i, z bands. Once convergence is achieved, a fraction of the flux in each pixel can be assigned appropriately to each object. The light of neighbours using the MOF models were subtracted off when running METACALIBRATION, in addition to using the überseg masking. Note the METACALIBRATION fitting only uses the MOF models to subtract neighbours.

We suspect that the überseg+MOF method may be more accurate than überseg-only, based on the performance in simulations (see Section 4.4.2). However, we use the überseg-only measurements in our fiducial catalogue, because photo-z measurements based on flux measurements from the artificially sheared images used in METACALIBRATION were not available for überseg+MOF at the time of writing. These are required in order to correct for selection effects

associated with placing galaxies into redshift bins, for example when studying shear correlations in tomographic bins.

We tested these two methods for flux assignment using both simulations and real data, as described in detail in the following sections. In brief, we find indications of relative shear biases at the 1–2 per cent level between our fiducial überseg and the MOF method of flux assignment, consistent between data and simulations.

4.4.1 Deblending tests in DES data

We compare tangential shear profiles around foreground galaxies, measured with our two different treatments of near neighbours described in Section 4.4. We use a simple ratio of the measurements as our test. As foreground galaxies we use the redMaGiC high density sample (Rozo et al. 2016) cut to the redshift range of $z = 0.2\ldots0.4$.

To reduce shape noise in the shear ratio, we perform the measurements with an identical source sample from the two catalogues. Note that with METACALIBRATION we can correct for selections as long as those selections are repeatable on quantities measured in artificially sheared images. We therefore apply the recommended cuts on flags, signal-to-noise ratio and pre-seeing size described in Section 7.2, demanding that they be met in both catalogues and correcting for the selection bias induced by the joint selection criterion. One selection in which we do not strictly adhere to this policy is source photo-z selection. As our source sample, we use galaxies with a BPZ photometric redshift estimate (Hoyle et al. 2018) based on their MOF photometry of $\langle z \rangle$ of 0.4 and above. While this could induce a small selection bias in our measurement, we do not expect it to significantly differ between the two catalogues, and we have confirmed that *not* applying a photo-z selection makes the resulting estimate of bias more noisy but consistent with our estimate.

We measure the tangential shear profiles from both catalogues in a set of jackknife resamplings of the full, matched source catalogue. For each jackknife resampling, we determine the best-fitting rescaling r required to bring the fiducial, überseg masked catalogue to the same amplitude as the MOF subtracted catalogue by minimizing

$$\chi^2 = \sum_i \frac{(g_{t,i}^{\text{MOF-subtracted}} - r \times g_{t,i}^{\text{fiducial}})^2}{\sigma_i^2} \, , \tag{19}$$

where $g_{t,i}$ is the mean tangential shear measured in a set of angular bins i, logarithmically spaced between 0.2 and 30 arcmin, from which the tangential shear around redMaGiC random points was subtracted to remove additive systematics, and σ_i is the jackknife uncertainty of $g_{t,i}^{\text{MOF-subtracted}}$. While the two estimates of tangential shear are highly correlated, this is meant to give an appropriate *relative* weighting to each radial bin. We test that swapping $g_{t,i}^{\text{MOF-subtracted}}$ and $g_{t,i}^{\text{fiducial}}$ in equation (19) or variation of the binning scheme does not change our constraints on r significantly, except for the inclusion of very small scales, on which fiducial shears fall off while MOF shears continue on a power-law-like profile, suggesting that MOF may be correcting for effects of blending with the lens galaxies.

These measurements are shown in Fig. 10. For a measurement involving all objects (blue data points), we find a relative multiplicative bias of the überseg shear catalogue of $m = 1 - r = 0.023 \pm 0.009$ (blue-shaded region).

If all of this difference is due to neighbour bias, we would expect this m to approach 0 as we limit the measurement to objects without many pixels contaminated by neighbours. We find that the ratio drops to $m = 0.018 \pm 0.015$ among galaxies with little contamination, selected as those with less than 10 per cent of area in their postage stamp masked for missing data or überseg neighbours
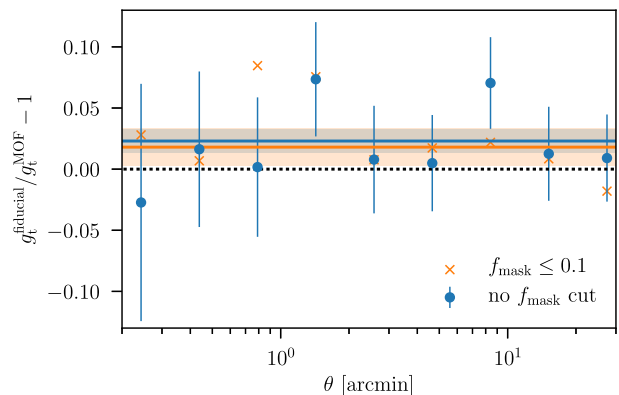
Figure 10. Ratio of shears measured with our fiducial METACALIBRATION pipeline to shears measured after subtracting neighbouring galaxies with model from the multi-object fit, a proxy for the multiplicative shear bias in either method due to the presence of neighbours. Blue data points show measurements for the full sample, including jackknife error bars of the fiducial run. Orange data points show measurements that only use objects with less than 10 per cent of area in their postage stamp masked for missing data or überseg neighbours. Blue and orange horizontal lines and shaded regions are the best-fitting m and statistical 1σ uncertainties for both cases. Marginalizing over an unknown multiplicative bias starts to dominate the posterior uncertainty in our main science use cases at about 2 per cent uncertainty.

(orange data points and shaded region). This ratio is no longer detected with high significance, but is consistent with both zero and the 0.023 ratio measured for the full sample.

We will test the effects of neighbours further using simulations in Section 4.4.2. Note that there will also be an effect from objects that are below the detection threshold, and thus not included in the catalogue. Studies using image simulations have shown that, when using simulations to calibrate the signal, neighbouring galaxies can indeed have a significant effect on multiplicative bias (Hoekstra et al. 2015; Hoekstra, Viola & Herbonnet 2017; Samuroff et al. 2018). We test this effect as well in Section 4.4.2.

4.4.2 Deblending tests in simulations

We used simulations to test the effect of blended objects, as well as objects fainter than the detection threshold. The motivation is to examine the relative performance of überseg and überseg+MOF, not to determine the numerical value of bias or to calibrate the shear measurements.

The simulations are similar to those used in Section 4.3 in the type of galaxy used, but include additional complexities. We used the same galaxy models described in Section 4.3, with a maximum magnitude for the COSMOS catalogue of approximately 25.2. In addition, we also added a lower flux population by simply scaling the flux such that the faintest magnitude was about 27.5, and scaled the sizes by a factor of 0.5. We also added a small number of big and high-flux objects by scaling the sizes by a factor of 5 and flux by a factor of 50. Approximately 85 per cent of the objects were in the low-flux category, and 0.1 per cent were in the high-flux category. Half the objects were sheared by 0.01 and half were sheared by 0.02, such that the mean shear was close to 0.015.

All images were convolved by a PSF modelled as a Moffat profile (Moffat 1969) with FWHM = 0.9 arcsec, and ellipticity 0.025 in the reduced shear convention. We added noise appropriate for 5-yr DES depths, such that the 5σ detection limit was about magnitude 24.

Table 1. Shear calibration bias *m* for METACALIBRATION in the deblending simulations. Shown are results when using the überseg algorithm to mask neighbours, as well as results when subtracting the light of neighbours using MOF models. Results are listed for three different threshold cuts in S/N, in addition to cuts at $T/T_{\mathrm{PSF}} > 0.5$ and SEXTRACTOR flags ≤ 3.

Method	S/N cut	m (10^{-2})
überseg	S/N > 10	2.18 ± 0.16
überseg	S/N > 15	1.73 ± 0.17
überseg	S/N > 20	1.74 ± 0.18
überseg+MOF	S/N > 10	0.10 ± 0.20
überseg+MOF	S/N > 15	-0.24 ± 0.21
überseg+MOF	S/N > 20	-0.04 ± 0.22

Note that most of the objects in these images are much fainter than the detection limit. Also note that these images are 'deeper' than Y1 data, with higher galaxy density. Thus, if the images matched real data exactly, we would expect the effects of neighbours to be larger than in Y1 data.

We generated images similar to DES coadds. We verified that the number density of objects in the resulting SEXTRACTOR catalogue matched that expected for DES data. We placed objects in the images randomly, with no spatial correlation. We found that the number of blends of detected objects is similar to that found in typical DES coadds field, but is not representative of fields with relatively low-redshift galaxy clusters. Thus these images are appropriate for testing cosmic shear measurements, but not necessarily for testing shear cross-correlations such as cluster lensing studies. Note that most of the galaxy images were well below the detection threshold, so there are a large number of undetected blends.

We then ran SEXTRACTOR on the images with settings similar to those used in DES, created MEDS files, and spatially matched the SEXTRACTOR catalogue to the input simulation catalogue, in order to associate a 'true' shear with each detection.

We ran the METACALIBRATION shear code on the MEDS files with identical settings used for the real data, including cuts on SEXTRACTOR flags ≤ 3, which only removes objects near edges or with incomplete apertures. Note that we cannot correct for this flag selection within the METACALIBRATION formalism. We then calculated the mean shear, which we compared to the mean 'true' shear from the matched catalogue. We ran in two different modes: one using the überseg algorithm only, and one subtracting the light of neighbours as measured using the MOF algorithm in addition to überseg masking.

The results are shown in Table 1 for a few different S/N thresholds, in addition to our fiducial size cut $T/T_{\mathrm{PSF}} > 0.5$ and SEXTRACTOR flags ≤ 3. When using überseg only we detect a ~ 2 per cent bias in all cases. We detect no bias when subtracting the light from neighbours.

For our default cuts (S/N > 10, $T/T_{\mathrm{PSF}} > 0.5$ and SEXTRACTOR flags ≤ 3) the ratio of biases for the two methods is approximately

$$\frac{1 + m_{\mathrm{useg}}}{1 + m_{\mathrm{MOF\text{-}sub}}} \approx 1.02. \tag{20}$$

This is consistent with the empirical bias ratio found in Section 4.4.1, but as noted above this simulation has a higher density of galaxies than Y1 data, so this may be an upper limit.

Because these simulations do not match the real data perfectly, we do not use these results to predict the systematic bias that may exist in either method for dealing with neighbours. Rather we treat these results as independent confirmation of the presence of a bias

between the two methods. It is suggestive that the bias may be higher in the fiducial überseg-only measurements.

4.4.3 Multiplicative bias prior due to blending

From the tests done on DES data and on simplified image simulations in the previous sections, we conclude the following

(i) The shear calibrations *m* of the MOF-subtracted and non-MOF-subtracted runs of METACALIBRATION differ at a level of $\Delta m \approx 0.023$, measured by the ratio of shear around lens galaxies with a matched version of both catalogues.

(ii) A Δm of the same sign but somewhat smaller amplitude remains when limiting the comparison to galaxies with little masking. The measured ratio 0.018 ± 0.015 is consistent with both zero and the 0.023 detected for all galaxies, and is thus inconclusive.

(iii) Although the image simulations do not match the data perfectly, and thus should not be used to estimate a numerical value for the bias, the results do give a bias difference of the same sign and comparable amplitude to the 1.02 value seen in equation (20).

The relative difference in multiplicative bias of the two runs of 0.023 can be interpreted in multiple ways. It could be that one of the methods is unbiased and the other is biased by 0.023. It is also plausible that neither method is unbiased, in which case the 0.023 is divided between the two methods. In order to encompass both scenarios, we adopt a Gaussian prior on the multiplicative bias of 0.012 ± 0.012, which is consistent with a bias of both zero and 0.023 at the 1σ level. We continue to use the überseg-only shear because photoz information is not available for the MOF-subtracted catalogue.

We note these numbers were derived directly from the data. For this reason we do not artificially increase the width of the prior as we did for numbers based on simulations.

4.5 METACALIBRATION and PSF modelling bias

The Y1 PSF modelling and interpolation exhibit small biases both in the size and shape (see Section 3), which result in additive and multiplicative errors.

The additive errors come about due to PSF mis-estimation, which results in inaccurate deconvolution during METACALIBRATION process, resulting in some remnant of PSF ellipticity remaining in deconvolved images of circular sources. We have calculated empirical estimates for the additive bias in the shear two-point correlation function as a function of angular separation (see Troxel et al. 2017), and shown that they are negligible once the mean shear is corrected.

We discuss multiplicative bias from PSF modelling errors in detail in Section 4.5.1. Additional biases due to stellar contamination in the source sample are discussed in Section 4.5.2.

4.5.1 METACALIBRATION shear bias from PSF modelling errors

As discussed in Section 3.2, our PSF model does not perfectly model the true PSF. Most aspects of the PSF modelling errors manifest as additive shear errors (see Section 6.2); however, the mean error in the size estimate of the PSF, described in Section 3.3, manifests as a multiplicative error. To measure the shear biases caused by these effects, we created further bulge+disc+knots simulations with a range of S/N, similar to those presented in Section 4.3 but using only a single simulated image per object.

We chose the minimum galaxy S/N used for these simulations to be S/N $\approx$ 50 in order to measure the shear bias at high precision. We saw no evidence that the magnitude of the effect depends on the galaxy S/N, so we expect these results to hold for our full galaxy sample including lower S/N objects.

We kept the nominal PSF model identical in all cases, using a Moffat profile with $\beta = 2.5$, a size corresponding to 0.9 arcsec FWHM, and $(e_1, e_2) = (0, 0.03)$. We then created several versions of the simulation with different true PSFs: (1) the same as the nominal PSF, (2) a constant PSF that was larger by $\Delta T/T = 8.3 \times 10^{-4}$, (3) a variable PSF with the correct mean size but varying in a normal distribution with $\sigma(T)/T = 3 \times 10^{-2}$, and (4) a variable PSF with both the larger mean and this variance.

The shears were measured with the same code used to process the DES data. We used the nominal PSF, not the true PSF, when performing the METACALIBRATION image manipulations. We applied various size cuts, and applied the appropriate shear and selection responses. For case 1 we found the bias to be less than 0.001 at 95 per cent confidence. This was expected because these simulations are similar to that presented in SH17, for which no bias was found. For case 2 with an overall PSF size error but no variance, we found a multiplicative shear bias of $m \approx 0.001$, independent of the size cut. With the additional size variance (cases 3 and 4) the mean bias increased, reaching nearly $m = 0.002$ for case 4. For case 4 the bias was independent of galaxy size for $T/T_{\mathrm{PSF}} > 0.3$, but we saw some variation for smaller sizes. This partly motivated the choice to cut at $T/T_{\mathrm{PSF}} > 0.5$ for our final shear catalogues.

We do not expect this simulation to produce an exact measure of the shear bias present in the real data, because it undoubtedly depends on the details of the morphology distribution of the galaxies and the precise distribution of the PSF errors around the mean value. We therefore attempt no correction for this effect. Rather, we take the results of this simulation as an estimate of a systematic uncertainty σ_m in the multiplicative error from this effect. We conservatively take the value of $\sigma_m = 0.003$. See Section 7.6.1 for a summary of all systematic uncertainties.

4.5.2 METACALIBRATION shear bias from stellar contamination

Stars do not bias METACALIBRATION shear recovery when the PSF is accurately known, since they should yield $\langle e \rangle = \langle R \rangle = 0$ (SH17). If, however, the PSF model is biased, stars will not have zero mean shear response $\langle R_\gamma \rangle$, which can potentially result in a shear bias. In Fig. 11 we show the decidedly non-zero response for known stars and galaxies in the COSMOS field. Such a distribution of responses for point sources will occur when the PSF estimate is biased, but the exact distribution depends intimately on the details of the PSF errors.

We can calculate the expected bias from these stars given our fiducial cuts S/N > 10 and $T/T_{\mathrm{PSF}} > 0.5$. Based on COSMOS we found this cut results in 0.4 per cent stellar contamination. Averaging over the stellar response distribution, and taking into account a re-scaling from the COSMOS stellar density to the mean density inside the DES Y1 footprint, results in a shear bias of $|m| < 0.001$. Because the COSMOS field may not be representative of the wider DES survey data, we take this measurement as indicative of the uncertainty in this systematic effect. We conservatively take $\sigma_m = 0.002$.
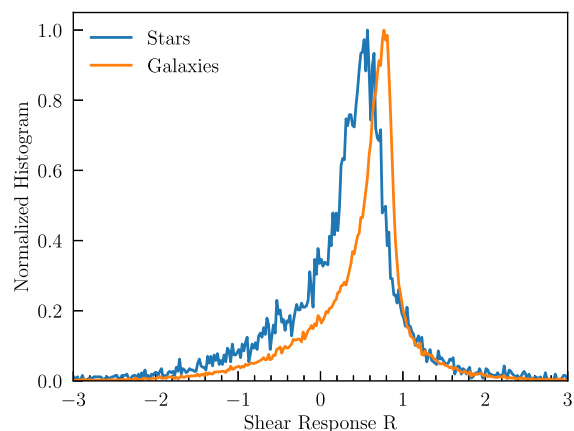
Figure 11. The distribution of responses measured in the COSMOS field for objects flagged as galaxies or stars. The non-zero response of the stars is due to noise in the measurement and interpolation of the PSF, and is accounted for in our error budget.

5 THE IM3SHAPE CATALOGUE

5.1 Overview

Our second DES Y1 catalogue was generated with the maximum likelihood code IM3SHAPE (Zuntz et al. 2013), which uses Levenberg–Marquardt minimization to find the maximum-likelihood (ML) fit of two Sérsic models, with power-law indices $n = 1$ and $n = 4$, to all the exposures of each galaxy simultaneously. Each galaxy is then identified as a bulge or a disc, depending on which model returned the superior likelihood.

The IM3SHAPE code[5] is largely unchanged from the version used for SV, though the simulations used to calibrate it have been upgraded significantly. We refer the reader to J16 and the original code release paper Zuntz et al. (2013) for code details.

The code fits six parameters: two ellipticity components (e_1, e_2), a half-light radius r, a centroid offset (x_0, y_0), and an amplitude A. For each fit we also compute a signal-to-noise ratio (S/N) using the convention of Mandelbaum et al. (2015) and J16. As we point out in J16, this signal-to-noise measure is analogous to a matched filter, favouring maximal agreement between the model fit and the image pixel fluxes. IM3SHAPE also defines a size metric $R_{\mathrm{gp}}/R_{\mathrm{p}}$, the ratio of the convolved galaxy FWHM to the PSF FWHM, where the former is measured from a circularized version of the best-fitting galaxy profile.

A small number of changes have been made to the code to improve internal organization, human readability, and tools for running it on high-performance computing systems. After these, the mean time taken to analyse a galaxy was 1.6 seconds per exposure, which was dominated by a small number of difficult objects. The total time was approximately 200 000 CPU hours for a single full analysis (not including the time taken for calibration simulations).

As noted in the introduction, maximum-likelihood methods such as IM3SHAPE accrue *noise bias* when the pixel values are a non-linear function of the model parameters, as is true in galaxy model fits. Along with all other sources of systematic measurement bias in our shear estimates, this effect must be calibrated. The most common approach, which we also adopt for Y1 of DES, is to do this using a suite of image simulations. We describe these simulations and the

[5]https://bitbucket.org/joezuntz/im3shape-git

calibration process used to generate the corrections needed for the data in Section 5.2.

All IM3SHAPE measurements presented here were carried out at the National Energy and Scientific Research Computing Center[6] (NERSC) and the GridPP grid computing system[7] (Britton et al. 2009). The calibration simulations were generated entirely using the NERSC facility.

5.2 The HOOPOE image simulations

We use a suite of simulations, called HOOPOE, to calibrate biases in the IM3SHAPE shape measurements. They account for noise bias, model bias, PSF leakage, mask effects, and selection biases. These simulations were used to model the m_i and c_i terms in equation (1). Previous studies have found no evidence of off-diagonal multiplicative bias when fitting Sérsic models, and we see no evidence of a systematic difference between m_1 and m_2 in any region of parameter space. Our calibration therefore uses the simple arithmetic mean $m = (m_1 + m_2)/2$.

Our Y1 simulations differ significantly from those used in SV. The latter started with postage-stamp images of isolated galaxies, to which we applied simulations of observational features. For Y1 we start with reduced image data from the survey, and create an object-for-object simulacrum, preserving as much of the original detail as possible. The differences are listed in detail in Table 2.

Variants of the HOOPOE simulations specifically to explore biases from blending are discussed further in Samuroff et al. (2018).

5.2.1 Simulating DES Y1: the image pipeline

The simulation pipeline for the HOOPOE image simulations is shown in the blue (left-hand) part of Fig. 1. The analysis of the resulting simulations was closely matched to the equivalent process used on real data, although we do not repeat the single-epoch data processing or PSF estimation stages. The position, noise levels, and PSFs of each simulated galaxy are taken from the real observations. The mask is made by combining the bad-pixel map, which is imported directly from real data, with the object segmentation map, which is remade on the simulations using SEXTRACTOR.

The HOOPOE image simulator begins by choosing one of the 0.73×0.73 deg coadd tiles output by the DESDM pipeline, each of which is generated by coaddition of around 70 partially overlapping exposures. For each tile we require (a) a source catalogue generated by SEXTRACTOR or similar object detection algorithm, (b) a WCS specifying the image bounds and the transformation between pixel and world coordinates per exposure, (c) a model describing the PSF variation across the image plane, (d) a noise variance weight map per exposure.

With these basic inputs the simulation then proceeds as follows for each sky region:

(i) Generate a set of noise images from the SEXTRACTOR weight maps, matched to the bounds of each data image. A simulated coadd-image is also generated in the same way.

(ii) Import the true detection catalogue for the region, and add to it a population of fainter undetected galaxies (see Section 5.2.4).

(iii) Iterate through positions, selecting a random COSMOS profile (from a rolling cache designed to make the expected number

of unique profiles per coadd tile 2000) and simulating it with additional shears and rotation angle drawn from $g_{1,2} \in [-0.08, 0.08]$, and $\theta \in [-\pi, \pi]$.

(iv) Convolve the profile with the PSF at the position in each image and draw it into each image (including the coadd).

(v) If a faint galaxy is associated with this position (see Section 5.2.4) then draw one from a secondary cache of faint profiles. It is placed in some point in the region formed by the overlap of all the exposures that contain the current galaxy, so that it will be in approximately the same geographic region as the primary galaxy but is not guaranteed to overlap it. It is sheared and convolved as in the previous steps.

(vi) Once the full image is simulated, run SEXTRACTOR on the simulated image, generating a new detection catalogue.

(vii) Iterate through the detection positions a second time, building the SEXTRACTOR mask for each and extracting a postage stamp cutout. In the version of the simulations presented here the stamp size was not recomputed for each object, but came from the size of the original object in the real images. Later code versions corrected this, but re-running the full simulations was deemed too expensive. The impact of this error is discussed in Section 7.6.2.

(viii) Store and stack the cutouts in the MEDS format (J16).

(ix) Run IM3SHAPE on the HOOPOE MEDS files, blinding using the prescription described in Section 2.6 with the same factor f as applied to the data.

5.2.2 Galaxy sample

To capture the range of morphologies found in a photometric survey like DES the Y1 HOOPOE simulations use real galaxy profiles rather than analytic constructions. In order to obtain an accurate calibration the profiles used as input should extend to at least the same depth as the data and have sufficiently low levels of noise and seeing to allow them to be degraded to match DES precisely, which limits the available data. We make use of the COSMOS sample described in Section 2.5, which meets these requirements.

We do not use the quality flags supplied with the COSMOS sample, which were not available at the time the code was run. Instead we visually inspected the sample, as described in Appendix A. The publicly available *HST* data are limited to wide band photometry in the optical *F814W* filter. In order to obtain the desired magnitudes in the DES bands, we match the sky position of each of these galaxies to the COSMOS mock catalogue of Jouvel et al. (2009), which includes photometry specific to the transmission curves of the DES filters.

The input sample for a tile is then generated by splitting the COSMOS catalogue about $M_{r,lim}$ and discarding objects too faint for detection. Each of these galaxies is simulated at its original COSMOS magnitude, rescaled to the zero-point of the DES images.

5.2.3 Simulated stars

The mock images also contain stars, simulated at the positions of objects classified as stars in the real data. Stars are rendered as point sources and account for around 10 per cent of simulated objects. This should capture any effect they may have as a source of neighbour bias, including changes they induce in the galaxy selection. We do not re-run star/galaxy separation in the simulations, so do not account for any mis-classification bias. The cuts to the IM3SHAPE catalogue in size and S/N, however, will remove the majority of the ambiguous objects, so we expect the impact of this

Table 2. Comparison of IM3SHAPE shear calibration schemes used in DES-SV and DES Y1. The upper portion of the table itemizes differences in the calibration simulations HOOPOE and GREAT-DES. Entries below the dividing line pertain to methodological choices rather than systematic differences between simulations. In the case of the interpolation scheme we compare three methods in this study, as described in the text below. The asterisks highlight the two interpolation methods used as the fiducial schemes in SV and Y1.

	GREAT-DES (DES-SV)	HOOPOE (DES Y1)
Multiple exposures	Coadd only	Multi-exposure
Point spread function	Discrete, Kolmogorov	PSFEx, image plane variations from data
Pixel noise	Gaussian random per pixel, fixed σ_n	Gaussian random per pixel, σ_n from weight maps
Blending/neighbours	None (postage stamp simulations)	Simulate full image plane
Galaxies below detection limit	None	Random positions, drawn from faint COSMOS cache
Source detection	None	Rerun SEXTRACTOR on simulated images
Masking	None	Spatial masks and PSF blacklists from GOLD catalogue
Input galaxy selection	COSMOS (<23.5 mag)	COSMOS deep (<25.2 mag)
Magnitudes/photometry	*HST F*814*W* magnitudes	SDSS (DES) *r*-band magnitudes
Stars	None	Point sources
Simulated galaxies	48M	68M
Input shears	$|g| = 0.05$, 8 discrete rotations	Continuous uniform random $-0.08 < g_{1,2} < 0.08$
Galaxy morphology	No morphology split	Bulges/discs calibrated separately
Interpolation/fit	Polynomial fit*	Grid nodes*
	Radial basis functions	Radial basis functions
		Polynomial fit
PSF measurements	IM3SHAPE weighted moments	HSM adaptive moments

decision to be small. For reference, the residual number of objects not removed by internal IM3SHAPE flags, but flagged as stars with the GOLD star–galaxy classifier in the data, is only about 1.5 per cent of objects.

5.2.4 Galaxies below the detection limit

In addition to simulating objects detected in real data we wish to simulate a population of fainter (undetected) galaxies. We choose a number of faint galaxies for each tile N_{faint} by integrating the full distribution of COSMOS magnitudes,

$$N_{\text{faint}} = \frac{f_{\text{faint}}}{(1 - f_{\text{faint}})} \times N_{\text{det}}, \qquad (21)$$

where $f_{\text{faint}} \equiv \int_{M_{r,\text{lim}}}^{\infty} p(M_r) \, dM_r$ is the fraction of the weight of the normalized magnitude distribution $p(M_r)$ above the nominal DES detection limit, and M_r is the aperture magnitude. In reality faint galaxies undetected by DES will include objects brighter than the nominal DES limiting magnitude, since the survey is really surface-brightness limited; the simple model here does not include this population, but should account for the leading order effect of faint neighbours.

Each of these extra objects is randomly assigned a companion from the detections within its coadd tile. This faint object is randomly placed into the same exposures as its detected companion, but does not replace it, nor are their properties linked in any other way.

In the real data the flux from these galaxies enters the images prior to reduction, and would affect the background subtraction. We choose not to simulate thermal sky emission and rerun the background subtraction. To gauge the impact of the extra background flux, we reran a small subset of the simulations with the same random seed settings, but without faint galaxies. The background estimation algorithm was then applied to the two sets of images, which were identical apart from the omission of the faint objects. To first order we find the sub-detection galaxies produce a uniform shift in the mean of the estimated sky background. To

correct for this effect, we subtract the average per-pixel flux of faint objects drawn into our simulated images.

The tests described here have neglected clustering between faint and bright galaxies, and between the faint galaxies themselves. Clustering would enhance the amount of blending, and would also make the sky subtraction effect more heterogeneous. Based on the variation of *m* with the density of faint objects we expect both of these effects to be smaller than the basic faint object effect described here, but not generally negligible. Future data sets will require simulations that include careful galaxy correlation modelling.

The impact of sub-detection galaxies on shear measurement is explored in more detail in section 5 of Samuroff et al. (2018). In the tests presented therein we find a net contribution to the multiplicative bias we correct for of $m \sim -0.01$ due to these sub-detection galaxies.

5.2.5 Comparing simulations and data

Given the sensitivities of measurement bias to the observable parameters of an image, most notably signal-to-noise, size, and ellipticity, it is important that the simulations should cover the same parameter space as the data. We explicitly calibrate over S/N and the ratio $R_{\text{gp}}/R_{\text{p}}$ of the galaxy image FWHM to PSF FWHM, so exactly matching simulations and data in these parameters are of secondary importance; matching the distributions of ellipticity, PSF size and shape, and other properties is more important for an accurate calibration.

The distributions of a selection of salient properties are shown in Fig. 12. Unlike in previous studies, we are convolving simulated galaxies with the measured PSF at each position on the sky, thus more directly matching the PSF variation across the sky compared to real data. Since we apply shape quality cuts it is not automatic that the PSF properties still match well to the data after those cuts – any significant difference in PSF properties *after* these cuts would imply a different selection behaviour with respect to PSF in simulations compared to the data. Unlike in real data the simulations do not include PSF errors, so we will be susceptible to the kinds of biases described in Section 4.5.1, which is also accounted for in our error budget (see Section 7.6.2).
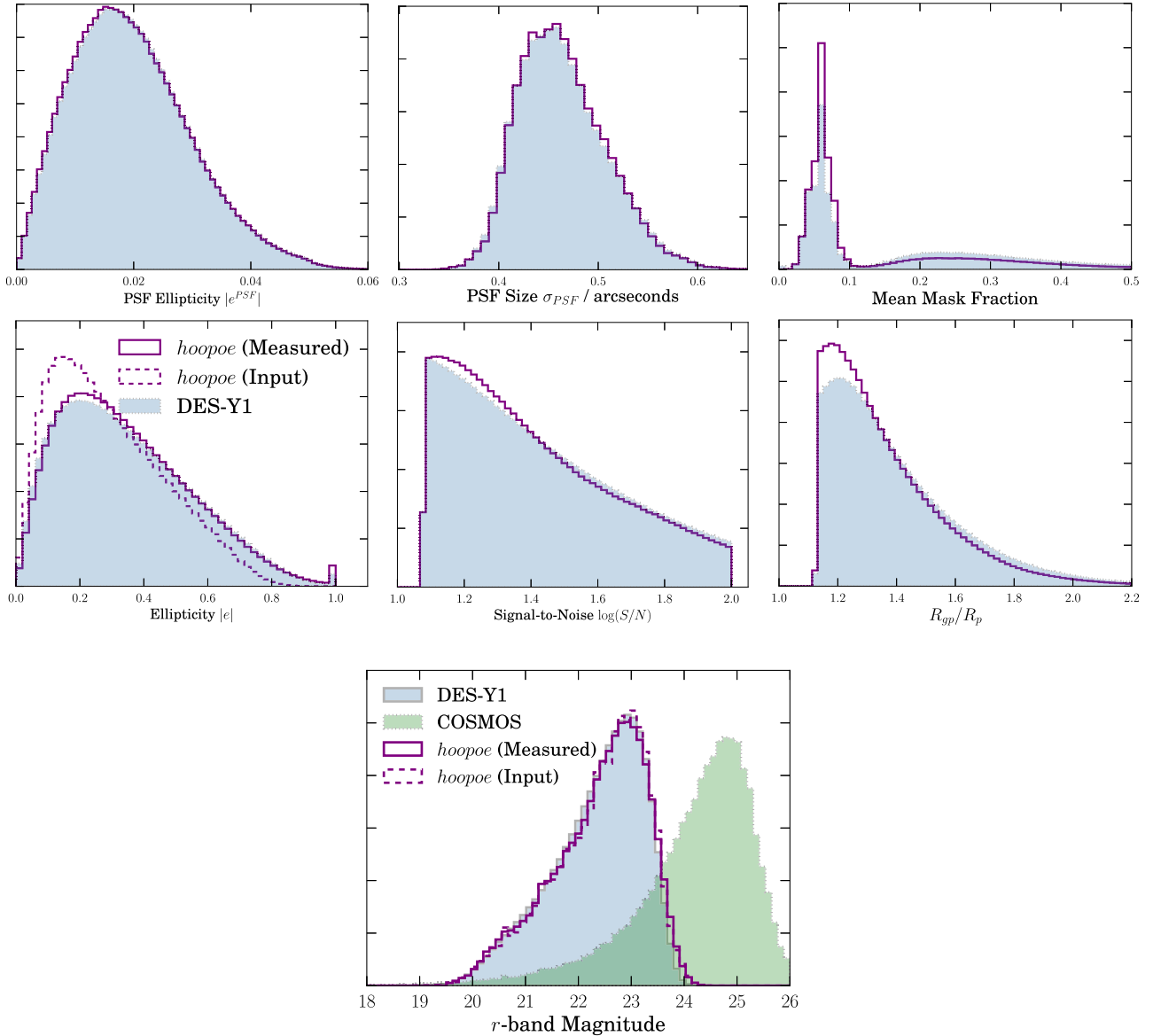
Figure 12. A comparison of normalized distributions in the Y1 simulations used for IM3SHAPE calibration (purple) and data (blue). The upper panels show (clockwise from upper left) PSF ellipticity; PSF size, as measured using HSM; the fraction of pixels masked out, averaged across each object's exposures; IM3SHAPE's measure of galaxy size relative to the PSF, R_{gp}/R_p; flux signal-to-noise; and total galaxy ellipticity. In the latter we show both the input and remeasured distributions to the simulations as dashed and dot–dashed lines, respectively. The lower-most panel shows the distribution of measured and input magnitudes from the simulation, in addition to the data. The shaded green (dotted) curve shows the equivalent r-band magnitudes for the full COSMOS catalogue from which we draw our input sample.

The distribution of *input* simulated ellipticities in Fig. 12 is notably narrower than the *measured* distributions in both simulations and data. As well as the expected effect of noise, this arises due to blending. An interesting comparison can be made with a new set of simulations, identical to HOOPOE, but with neighbour light removed (described in Samuroff et al. 2018). In those simulations we find that the measured ellipticity histogram is much closer to the input distribution.

As in J16, the difference in R_{gp}/R_p increases at small sizes. This may be due to the COSMOS sample used, or the similar PSF estimation methodology.

Finally in the lower panel we compare the input and output magnitudes from the simulations. We do not find a significant bias in the remeasured magnitudes, nor serious disagreement with the data.

Though most properties match well, there are obvious inaccuracies in the simulated R_{gp}/R_p and flux distributions. In Appendix B we test their impact by reweighting the simulation to match the data, and find no significant change in the final calibration. In Appendix C we describe tests of the impact on the calibration of other features in the simulations that differ from the data.

5.3 Bias calibration and diagnostics

5.3.1 Multiplicative bias scheme

We now define a scheme to correct for the multiplicative bias measured in the simulations, which must interpolate among the very noisy individual measurements. Both on theoretical grounds for noise bias (Refregier et al. 2012) and in practice for general biases (J16, Fenech Conti et al. 2017), the galaxy size and S/N parameters are the dominant factor in determining bias. We therefore build a calibration model in terms of those parameters.

The first step in this process is to decide on the most relevant parameters upon which the measurement biases depend, and calculate m, c_i as a function of those parameters. To this end, we sort the simulated HOOPOE data into a 16×16 grid according to the measured S/N and R_{gp}/R_p, allowing the bin width to vary such that each grid cell contains roughly the same number of galaxies. A multiplicative bias is derived within each cell by subdividing the galaxies into bins of g^{tr} and fitting a linear function to the bin-averaged shear response $\langle e_i \rangle - \langle g_i^{tr} \rangle$ (see equation 1). The resulting bias surface m^{ij} is shown in Fig. 13.

It is important here to define a well-motivated gridding scheme in terms of bin numbers along each axis; too coarse a grid will result in real structure in this parameter space being washed out, while an overly fine sampling will inflate the statistical variance on our grid nodes. We have verified that varying our fiducial 16×16 grid between 6×6 and 20×20 does not lead to a significant change in the results.

We compare three methods for interpolating between grid nodes. In the first scheme, we follow Fenech Conti et al. (2017), and compute a fine grid in m. If a galaxy falls within cell ij, we simply take the mean m in that cell as our bias estimate. The accuracy of such an approach will depend on the resolution of the grid.

In the second scheme we interpolate with radial basis functions. The bias at a point is a linear combination of radial basis functions, each centred on one of the grid nodes:

$$m(x, y) = \frac{\sum_i m_i f((x - x_i)^2 + (y - y_i)^2)}{\sum_i f((x - x_i)^2 + (y - y_i)^2)}, \tag{22}$$

where

$$f(r^2) = \left(r^2/\epsilon^2 + 1\right)^{-\frac{1}{2}} \tag{23}$$

and the (x, y) coordinates are S/N and R_{gp}/R_p suitably weighted to give the two dimensions parity, ε is a fixed smoothing parameter, and the sums are over the grid nodes.

Finally, we fit the polynomial basis used in J16. We will not write out the entire functional form here, but note that it consists of a linear combination of 18 terms of the form $(S/N)^{-\alpha}(R_{gp}/R_p)^{-\beta}$, where the indices α, $\beta \in (1.25, 1.5, 1.75, 2, 2.5, 3, 4)$. We will refer to these three methods respectively as *grid*, *RBF*, and *polynomial* calibration schemes. Owing to slightly better performance in diagnostic tests the grid scheme is our fiducial choice.

The relative performance of the three schemes is shown in Fig. 14, where we show the residual bias after calibration as a function of signal-to-noise and galaxy size. The grid model is constructed using two sets of equal-number cells, defined for bulge and disc galaxies independently. The bin edges used to evaluate it are defined by the full catalogue, and so are not identical.

5.3.2 Robustness to tomographic binning

A simulation-based calibration of the sort presented here may be valid for the full dataset, and yield residual biases within tolerance, but it does not trivially follow that this is true for all sub-divisions of the data. It is perfectly possible that there are competing sources of biases in the catalogue, which by chance cancel to zero. It is also possible to induce biases by introducing extra post-calibration selections based on quantities which correlate with galaxy shape. We will show an explicit example of this in Section 7.3.

Many science applications of the Y1 shape catalogues require a calibration that is robust to selection in bins of redshift and angular scale. HOOPOE uses input galaxies with redshifts and generates images in sky coordinates, allowing us to test both of these. In this section we focus on the tomographic selection; we refer the reader to Samuroff et al. (2018) for discussion of scale-dependent selection effects.

The redshift information we use for each COSMOS galaxy has the form of single point-estimate photo-z, as estimated using the ACS 30-band photometry. In the following we assume this measurement is of sufficient quality to allow us to treat it as an input 'true' redshift z_{tr}.

We build two sets of tomographic bins for the simulated dataset. For the first set we use the COSMOS measurement z_{tr} for each object; this corresponds to an ideal situation in which we have no redshift error and sharp-edged (top-hat) redshift bins. In the second set we mimic the scatter in photometric redshift that will inevitably be present in DES. Each HOOPOE galaxy is stochastically allocated to one of the four Y1 redshift bins as follows. First we construct a realistic set of DES Y1 redshift estimates using the Y1 IM3SHAPE catalogue. The per-galaxy redshift PDFs obtained from the BPZ code are stacked in four bins $z = [(0.2-0.43), (0.43-0.63), (0.63-0.9), (0.9-1.3)]$, resulting in four normalized distributions $n^i(z)$. We assign each galaxy with true redshift z_{tr} to a bin i, with probability $n^i(z_{tr})/[\sum_{j=1}^{4} n^j(z_{tr})]$. The resulting histograms of z_{tr} in each bin cover the full range $z \in [0.2-1.3]$, and approximately match the measured $n(z)$ in that bin from the data. This random assignment of redshifts is a simplified model; it does not simulate systematic correlation between photometric redshifts and shear, but it does address the smearing out of the estimated redshifts due to noise, which we expect to be dominant.

To test the redshift dependence of our calibration, we measure the residual bias after splitting into these bins. The results are shown in Fig. 15 and Table 3 (the latter includes values for the alternative interpolation methods). The top-hat results show larger RMS scatter than those using the more realistic redshift binning, which blur out the bias slightly.

The residuals in our top-hat redshift bins demonstrate an important limitation of our current calibration procedure: namely that galaxy morphology (and thus measurement bias) varies with redshift. Our calibration assumes that S/N and size are a sufficient proxy for change, which will be true only to some level of accuracy. The results on DES-like photometric bins suggest this will have less impact on our real data. We have also neglected noise effects which would induce correlations between both redshift, via fluxes, and ellipticity. For higher precision calibrations on future data both of these issues must be addressed.
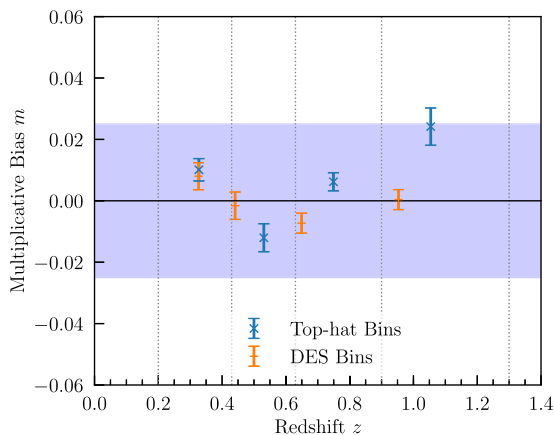
As a further test, we split the calibration sample into halves, and then use each half to generate a calibration model for the other. We perform this test twice, once completely at random, such that each part contains an equal number of HOOPOE galaxies, and once by
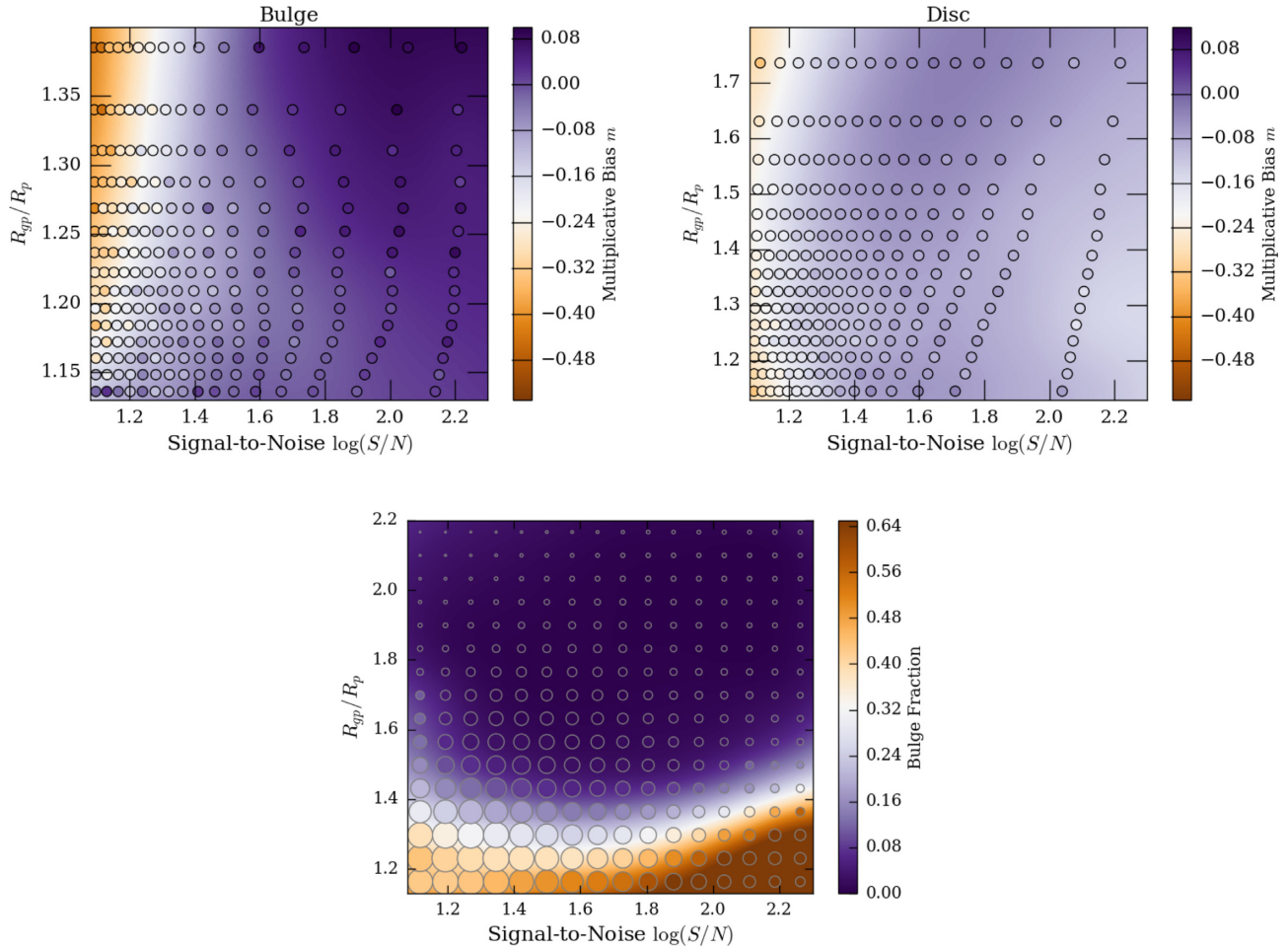
Figure 13. Top: Multiplicative bias estimates for Y1 IM3SHAPE, using the HOOPOE image simulations for objects fitted using bulge profiles (right) and disc profiles (left). The coloured circles represent the grid of directly evaluated m described in the text. The underlying colour map is generated using radial basis functions to interpolate between nodes, and is for illustrative purposes only. **Bottom:** Bulge fraction as a function of galaxy signal-to-noise and size. The bulge fraction is calculated on a 16×16 grid and interpolated to generate the smooth map shown. The circles represent the grid cell positions, and are drawn at a size proportional to the total IM3SHAPE lensing weight of galaxies contained.
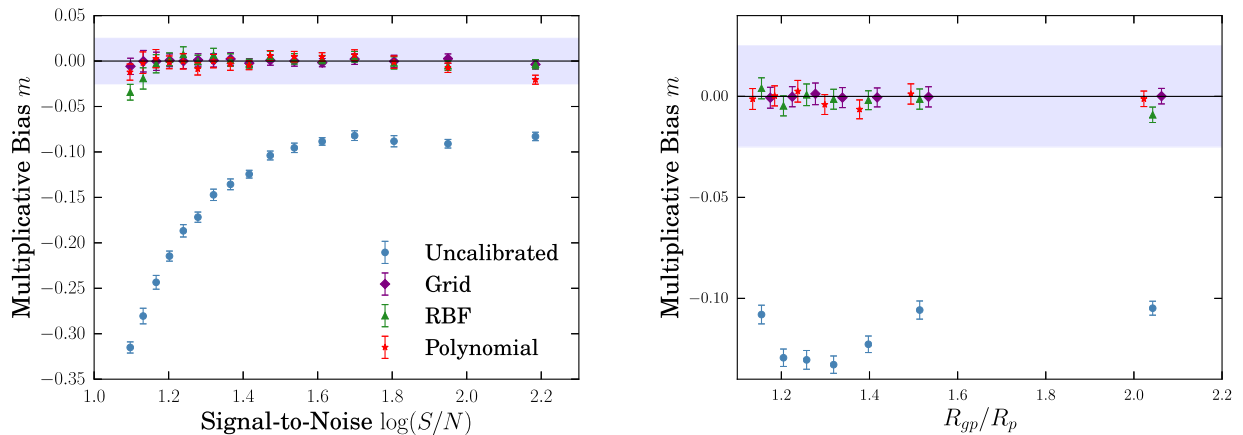
Figure 14. Multiplicative bias for IM3SHAPE measured from the full Y1 simulations, as a function of galaxy signal-to-noise and size. The blue circles in both panels are the measured biases prior to calibration. The other points, labelled grid, RBF, and polynomial are the result of correction using the three methods described in the text. The shaded band marks the $\pm 1\sigma$ Gaussian width of the recommended m prior for the Y1 IM3SHAPE catalogue.

5.4 Galaxy weights for IM3SHAPE

We compute an IM3SHAPE measurement weight for each galaxy using a very similar calculation to that used in J16. In summary, we first define a 2D grid of signal-to-noise and size, with each cell containing roughly the same number of galaxies. In each cell a zero-centred Gaussian is first fitted to the histogram of the e_1 component ellipticity, and the stand ard deviation is also calculated directly. This yields two similar but non-identical variance estimates, of which we adopt the maximum. The resulting grid is then interpolated using 2D radial basis functions, and the weight allocated to a given galaxy is simply the inverse of the interpolated variance at that position. This process is designed to estimate the total uncertainty of an ellipticity measurement, including both shape noise and measurement uncertainty, or $(\sigma_e^2 + \sigma_{SN}^2)$ in the syntax of J16 Section 7.3. Simulated galaxies were assigned weights by the same process, which were used in constructing the calibration.

6 TESTS OF THE SHEAR MEASUREMENTS

Lensing null tests can be difficult to construct, because of strong correlations (both inherent and noise-induced) between measured shear and other measurable observables.

None the less they remain a powerful tool when correctly understood. These null tests can be broken up into several broad categories:

Spatial tests check for systematic errors that are connected to the physical structure of the camera. Examples of these are errors in the WCS correction, including effects like edge distortions or tree rings (Plazas, Bernstein & Sheldon 2014a), and errors related to features on the CCDs such as the tape bumps. (Section 6.1)

PSF tests check for systematic errors that are connected to the PSF correction. This includes errors due to inaccurate PSF modelling as well as leakage of the PSF shapes into the galaxy shape estimates. (Section 6.2)

Galaxy property tests check for errors in the shear measurement algorithm related to properties of the galaxy or its image. This can include effects of masking as well, which involve the other objects near the galaxy being measured. (Section 6.3)

B-mode statistics check for systematic errors that show up as a B-mode signal in the shear pattern. The gravitational lensing signal is expected to be essentially pure E-mode. Most systematic errors, in contrast, affect the E- and B-mode approximately equally, so the B-mode is a direct test of systematic errors. (Section 6.4)

Cross-catalogue comparisons check that the two shear catalogues are consistent with each other. It has previously proven extremely challenging to test the agreement between two catalogues directly, because of the calibration corrections that are required when selecting any given subset of a catalogue. In particular, the METACALIBRATION selection bias correction in equation (17) requires executing any selection cuts on the sheared renditions of the galaxy images. It is impractical to run IM3SHAPE in this context, and even less so to incorporate METACALIBRATION cuts into the IM3SHAPE bias correction simulations. This makes it impractical to use direct shear comparisons, either object-by-object or on populations, to compare the catalogues.

The best cross-catalogue comparison we can make is therefore to compare the results they yield at the 'science' level, such as cosmological parameter constraints from shear-shear or galaxy-galaxy lensing. These tests are described in accompanying papers (DES Collaboration 2017; Prat et al. 2017; Troxel et al. 2017). Considering the large differences between the METACALIBRATION and

Figure 15. Residual multiplicative bias for IM3SHAPE measured from the full HOOPOE catalogue in four tomographic bins after fiducial calibration. For the 'Top-hat' points objects are binned by their COSMOS redshifts, and for the 'DES' bins they are assigned to match DES Y1 redshift distributions, partially simulated photometric redshift errors. As above the shaded band shows the 1σ width of our Gaussian prior on m in the Y1 IM3SHAPE catalogue, and the vertical dotted lines show the redshift bin boundaries.

Table 3. Residual multiplicative bias in the IM3SHAPE calibration simulations, after calibration using different methods for interpolating m^{ij} nodes onto individual galaxies. The calibration is derived globally, and the residuals are computed for the redshift bins used in the cosmic shear analysis in Troxel et al. (2017).

Method	$\Delta m^{(1)}$	$\Delta m^{(2)}$	$\Delta m^{(3)}$	$\Delta m^{(4)}$
Uncalibrated	-0.0886	-0.0981	-0.1200	-0.1547
Grid	0.0069	-0.0014	-0.0074	0.0013
Radial Basis	0.0056	-0.0024	-0.0082	-0.0022
Polynomial	0.0049	-0.0028	-0.0078	-0.0000

profile, such that each part contains half of the unique COSMOS profiles used. Since the biases will depend on both the distribution of galaxy morphologies and the specific observing conditions in the calibration sample, both these tests are relevant. The results are shown in Table 4.

Though subdominant to the other forms of systematic bias discussed in this paper, the residual bias in the third redshift bin is statistically significant. Some residual biases might be expected, given that we are using a rigid two parameter grid to describe complex morphology-dependent biases. Unfortunately it is not possible to predict the magnitude or sign of these residuals, which depend on the details of the COSMOS sample and how they are distributed between redshift bins. It is thus not guaranteed that the measured residual m in the third redshift bin implies an equivalent bias in the data.

To account for this uncertainty we widen our prior on m after calibration. The maximum amplitude of the residual bias in Fig. 14 is $|\Delta m^{(i)}| = 0.0074$. We include this amplitude rounded up to $\sigma_m = 0.01$ as a systematic contribution to the prior on residual bias in the IM3SHAPE catalogue (see Section 7.6). To be conservative, we also widen the m prior to account for the fact that these residual biases will be correlated between redshift bins (Appendix D).

Table 4. Residual multiplicative bias in the HOOPOE simulations under various divisions. For reference the top line shows the result of applying the fiducial calibration to the whole catalogue, and is identical to the 'grid' line in Table 3 and the purple diamonds in Fig. 14. The other lines show the remeasured biases when using disjoint calibration and validation subsets of the simulation. We split first at random, such that there are equal numbers of HOOPOE galaxies in each subset, and then such that there are equal numbers of COSMOS profiles in each.

Split type	$\Delta m^{(1)}$	$\Delta m^{(2)}$	$\Delta m^{(3)}$	$\Delta m^{(4)}$
None	0.0069 ± 0.0044	-0.0014 ± 0.0046	-0.0074 ± 0.0030	0.0013 ± 0.0034
At random	0.0021 ± 0.0046	-0.0018 ± 0.0039	-0.0095 ± 0.0039	-0.0027 ± 0.0054
By COSMOS profile	0.0034 ± 0.0062	-0.0006 ± 0.0060	-0.0048 ± 0.0037	0.0073 ± 0.0039

IM3SHAPE codes, these are very stringent tests, especially since no tuning or modification of any kind was performed to ensure agreement of the results from the two codes. Agreement in cosmological parameter constraints demonstrates the agreement of the catalogues for one specific scientific use case, not general agreement in other areas.

6.1 Spatial tests

Several sources of error related to the variation in pixel behaviour and response across the CCDs might, if not properly accounted for, leave an imprint on the shape catalogue. These could include silicon 'tree rings' (Plazas et al. 2014a), CCD defects and bad columns, and a 'glowing-edge' effect in which the pixels at the edges of the CCDs have a different effective size to those in the bulk. To search for these effects we can bin the catalogues in pixel and field-of-view coordinates. We can also plot mean shears in radial bins around the central points of exposures and CCDs – if all is well these points should have the same signal as randomly chosen points.

Another potential spatial bias comes from the effects of masks in the data, which can have a preferred direction. Columns of CCDs, for example, are often masked out together, and diffraction spikes orient with the optics of the telescope. The DES focal plane does not rotate, so these effects always correspond to the same orientation in sky coordinates. This can affect shape measurement of galaxies near the edge of the mask in two ways – a selection effect on their detection since objects aligned perpendicularly to the mask are more likely to have pixels removed, and on the measurement of their signal-to-noise, for a similar reason. The latter effect, which is expected to be larger, is included in the METACALIBRATION response function and the IM3SHAPE simulations. The exposure dither means that if a galaxy is masked in one exposure it is generally not in others; this reduces the size of the former effect. No detection selection bias is seen in simulations with real masks.

6.1.1 Position in the field of view

Fig. 16 shows the mean ellipticity for each pixel in the focal plane, binned across all exposures. No trends or problematic regions are visible in the plot, which is consistent with noise.

6.1.2 Tangential shear around field centres

Fig. 17 shows the tangential shear binned by radius around field centres (the set of points where the centre of the focal plane is pointing over all exposures) of the Y1 survey. The mean tangential shear around a comparable number of randomly selected points is subtracted before plotting. No significant difference is seen at separations $\theta < 200$ arcmin, but on larger scales we see a significant deviation of γ_t up to 10^{-5} around the centres (note that figure shows $\theta \gamma_t$). We verify in Prat et al. (2017) that this contamination is not a

significant contaminant to the cosmological γ_t signals in our bins; other users of these catalogues should perform similar tests for their science case.

6.2 Tests of the PSF correction

6.2.1 Shear–PSF size correlation

Fig. 18 shows the mean shear in galaxies in bins of the size of the PSF for the two catalogues, each using its own size metric. In each case a mean shear is visible, which is discussed further in Section 7.1. The mild trend in e_1 is negligible compared to our measured results.

6.2.2 Shear–PSF ellipticity correlation

Fig. 19 shows the mean estimated shear in bins of PSF model ellipticity. The clearly detected correlation between shear and PSF ellipticity can be an indication of imperfect deconvolution of the PSF from the galaxy image, or of simply imperfect modelling of the PSF. Paulin-Henriksson et al. (2008) demonstrate that size errors in the PSF model can potentially produce an additive bias in the shear in the direction of the PSF ellipticity.

The trends in Fig. 19 can also be produced when there is a correlation between the PSF ellipticity and the PSF model ellipticity errors (i.e. a non-zero ρ_2, see Section 3.3). We find that while in this case PSF model size errors do not significantly contribute to Fig. 19, the PSF model ellipticity errors (and their correlation with the PSF model ellipticity) do. We split up the α term in equation (2), into a 'true' α from imperfect deconvolution and a term β from imperfect measurement:

$$c_i = \alpha_i p_i + \beta_i q_i, \tag{24}$$

where p_i is component i of the PSF model ellipticity and q_i is component i of the PSF model ellipticity error, i.e. $q_i = p_i - p_i^{\text{true}}$. For perfect deconvolution, we expect $\alpha = 0$. On the other hand, we expect β to be of order -1 for any shape measurement algorithm, since an error in the PSF model ellipticity will propagate to an error of the same order of magnitude, but opposite sign, in the inferred shear (see Paulin-Henriksson et al. 2008 for a theoretical estimate of the linear order effect of PSF size and ellipticity errors).

While we can estimate the PSF model ellipticity errors q_i at the position of stars, we do not have an estimate at galaxy positions, so we cannot directly estimate the coefficient β. However, we can use the fact that PSF modelling errors are spatially correlated either in focal plane coordinates (as demonstrated in Fig. 8) or in sky coordinates (as demonstrated by the non-zero ρ_1 in Section 3.3). We take advantage of the former by computing a PSF ellipticity residual estimate for each galaxy in our sample by interpolating the ellipticity residual maps at Fig. 8 to the focal-plane positions where the galaxy appears. We average this quantity over the multiple
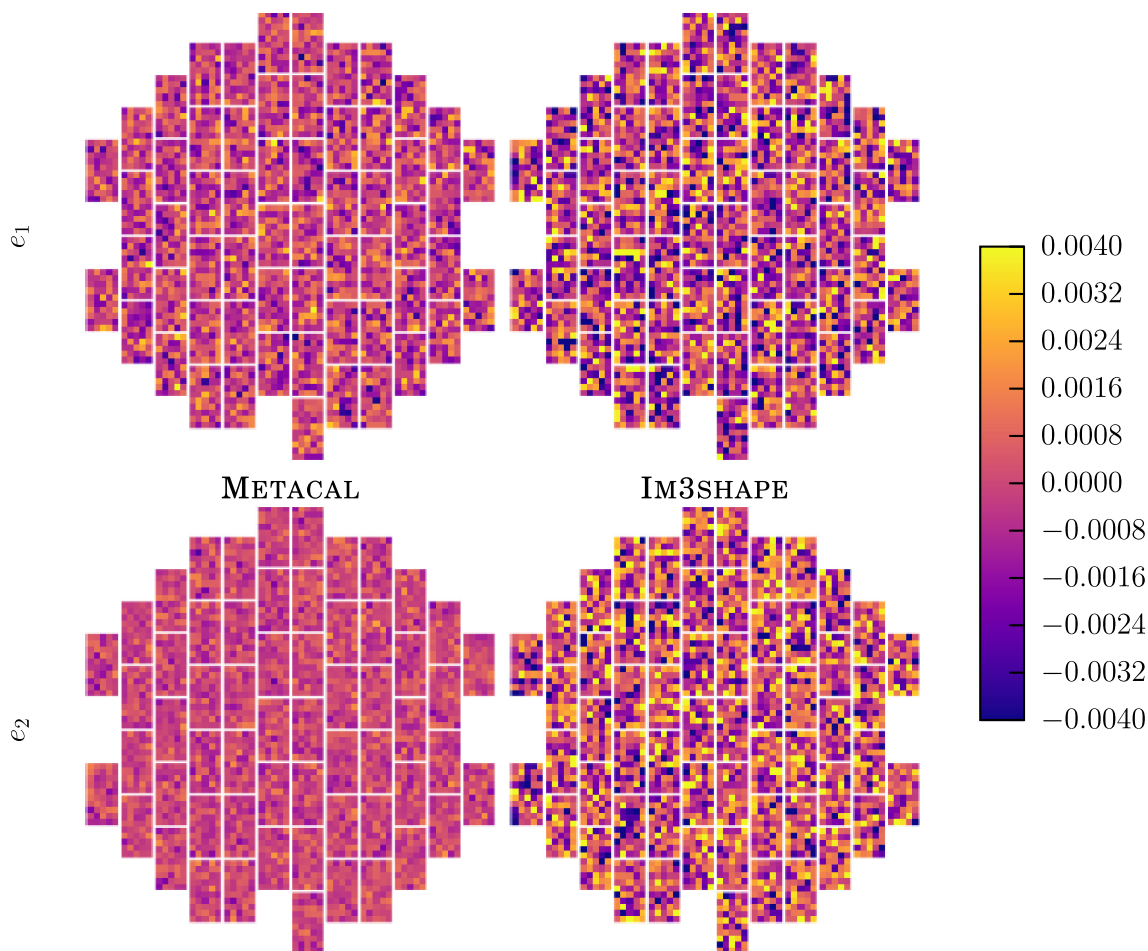
Figure 16. The mean ellipticity for METACALIBRATION (left) and IM3SHAPE (right) binned by position in the focal plane. Each bin is approximately 400 pixels across. The IM3SHAPE catalogues use only *r*-band data and so are noisier.
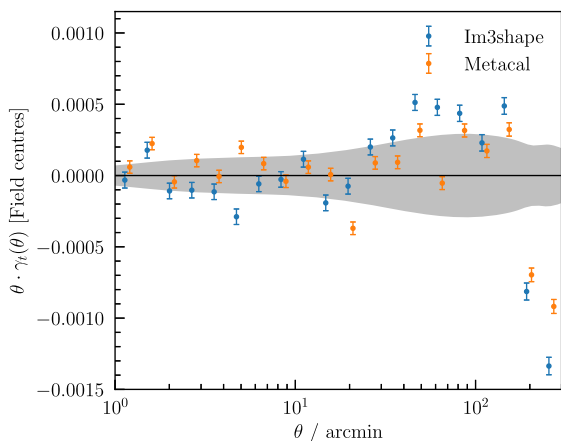

Figure 17. The tangential shear of galaxies in the two catalogues around field centres, after subtraction of shear around random points. The grey band shows 10 per cent of the weakest tangential shear signal around galaxies in any of the galaxy–galaxy lensing measurements used in Prat et al. (2017). This weakest signal combination was from lens bin 3, source bin 4; the data from this combination were used only at $\theta > 30$ arcmin. As noted in the text the deviations from nullity are significant, and a further test was done to ensure that they did not impact our galaxy-galaxy lensing science.
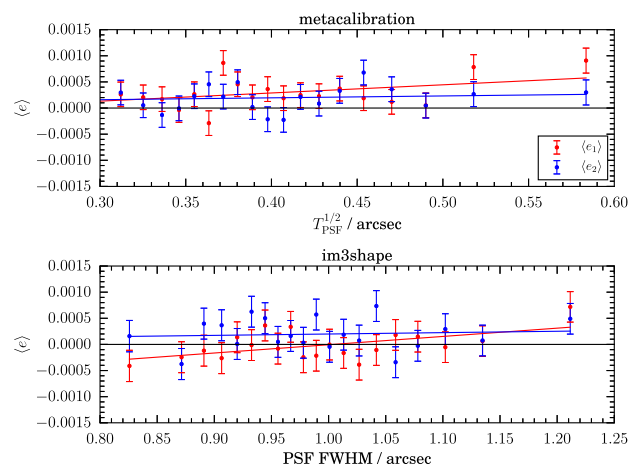
Figure 18. The mean galaxy shear as a function of the input PSF size (METACALIBRATION top and IM3SHAPE bottom). The solid lines are linear best fits to the data points.

focal plane positions at which each galaxy was observed; call this $\bar{q}_i$. We can then compute the correlation of this quantity with the inferred shear; this is shown in Fig. 20. For both components, the
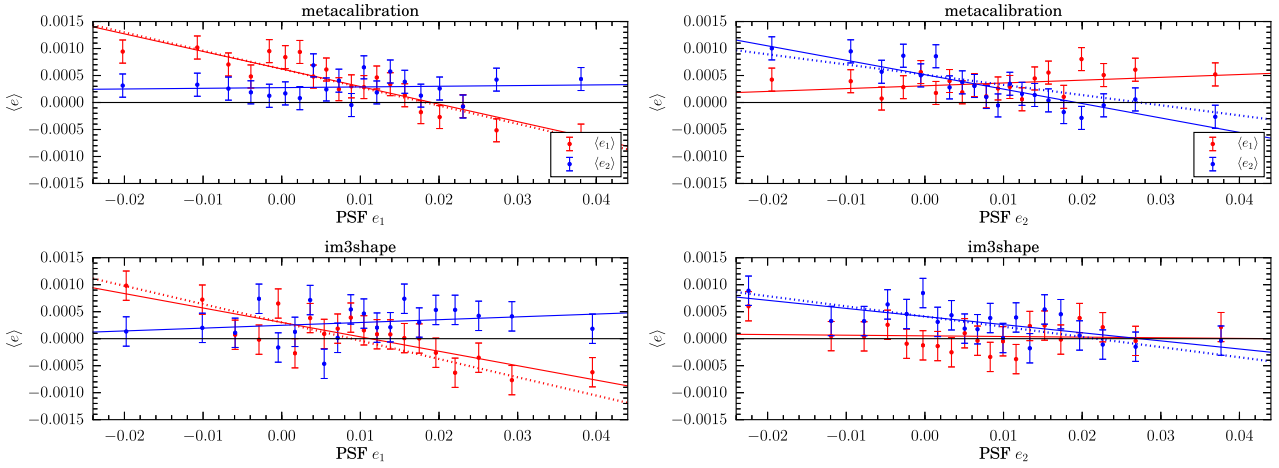
Figure 19. The mean galaxy shear as a function of the input PSF ellipticity (PSF e_1 left, and PSF e_2 right; METACALIBRATION top, and IM3SHAPE bottom). The PSF ellipticity means and limits for both catalogues are not identical. This is partly due to METACALIBRATION using exposures from all three *riz* bands, while IM3SHAPE is limited to the *r* band. Different models are also used to measure the PSF ellipticity in both catalogues. The solid lines are linear best fits to the data points. The $e_1(p_1)$ and $e_2(p_2)$ terms have non-zero slopes that are consistent between the two catalogues, and are consistent with the dotted lines, which come from a model in which all the variation with PSF arises from mis-estimation of the PSF, rather than in the shape measurement directly. The dotted line slopes are $\partial e_1/\partial p_1 = -0.030$ and $\partial e_2/\partial p_2 = -0.018$.
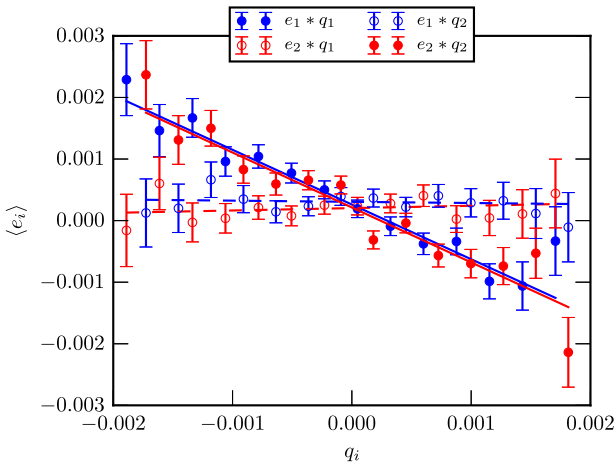
Figure 20. The mean shear $\langle e_i \rangle$ as estimated by METACALIBRATION as a function of focal-plane-position-averaged PSF ellipticity model residual q_i, for each pair $i = (1, 2)$ for each quantity. See Section 6.2.2 for a description of this latter quantity.

Figure 21. Tangential shear around stars, which have been split into a bright ($14 < m_i < 18.3$) and a faint sample ($18.3 < m_i < 22$). The faint sample includes stars used for PSF modelling while bright stars are used to test other effects related to the saturation around them. The error bars come from the jackknife method. The grey band is 10 per cent of the weakest expected signal, as in Fig. 17. The deviations from null in this test at small scales were excluded by the scale cut $\theta > 30$ arcmin.

slope (which in our model is given by β) is indeed $O(-1)$ ($\beta_1 = -1.08 \pm 0.08$, $\beta_2 = -1.05 \pm 0.07$).

With this estimate of β in hand, we can then estimate the contribution of PSF model ellipticity errors to the correlation between shear and PSF model ellipticity in Fig. 19. Assuming $\alpha = 0$ we expect a slope

$$\frac{\partial e_i}{\partial p_i} = \beta_i \frac{\partial q_i}{\partial p_i}. \qquad (25)$$

We estimate the derivative on the right hand side using the ellipticity measurements of the 'reserved' stars described in Section 3.3. We find an expected contribution to the slope of δe_i vs. e_{PSF} as shown in Fig. 19 of $\frac{\partial e_1}{\partial p_1} = -0.030$ and $\frac{\partial e_2}{\partial p_2} = -0.018$ for two components in METACALIBRATION. For both the catalogues the overall leakage from PSF to shear is explained well by this term alone.

6.2.3 Tangential shear around stars

Since stars will not act as effective gravitational lenses of distant galaxies the measurement of tangential shear around them provides a null test that can reveal problems that could potentially contaminate the galaxy–galaxy lensing signal. In particular, the tangential shear around faint stars, which includes objects used to constrain the PSF modelling, can be used to check issues with PSF modelling and interpolation. On the other hand, bright stars are not used in the PSF modelling but can induce problems around them due to blending and pixel saturation. We define the bright/faint cuts from J16, with $14 < m_i < 18.3$ for the bright sample and $18.3 < m_i < 22$ for the faint one.

The results of these tests are shown in Fig. 21, for both METACAL-
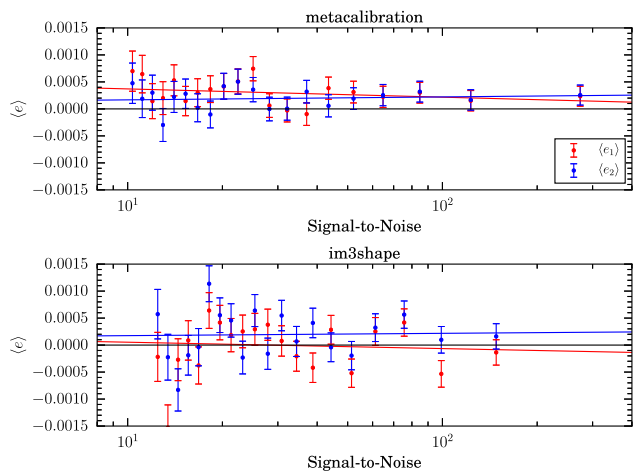
Figure 22. The mean galaxy shear as a function of the signal-to-noise (METACALIBRATION top, and IM3SHAPE bottom). The solid lines are a linear best fit to the data points.

IBRATION and IM3SHAPE. We find the signal to be consistent with zero in all cases, using the covariance from jackknifing the stars.

6.3 Galaxy property tests

6.3.1 Galaxy signal-to-noise

Fig. 22 shows the mean ellipticities e_1 and e_2 after calibration for the two catalogues in bins of measured signal-to-noise. The S/N value for each catalogue comes from its own measurement process, and different cuts have been applied, so the galaxies in corresponding bins are not identical.

The IM3SHAPE calibration process uses signal-to-noise as a calibration parameter, so after calibration the mean shape should be uncorrelated with signal-to-noise. The METACALIBRATION calibration process should also remove any correlation. Any physical correlations between shape and brightness should have no preferred direction, and therefore should not appear in Fig. 22.

Neither catalogue shows a strong trend in shear with S/N. Both catalogues have a non-zero mean shear which is visible here and discussed in Section 7.1.

6.3.2 Galaxy size

In IM3SHAPE the size of source galaxies is measured by R_{gp}/R_p as described in Section 5.1, and in METACALIBRATION we measure it as $T^{\frac{1}{2}}$, where T is defined in equation (3). In neither case should any correlation between the size and ellipticity be present after applying the calibration process. Fig. 23 shows mean galaxy ellipticity as a function of the size metrics. In neither case do we see any significant trend in ellipticity as a function of galaxy size.

6.4 B-mode statistics

In general relativity (GR) lensing produces an E-mode (curl-free) pattern in the shear field, and no detectable B-mode (divergence-free) pattern. Contaminants to the signal such as PSF or other leakages might produce either mode, so if we assume GR we can use
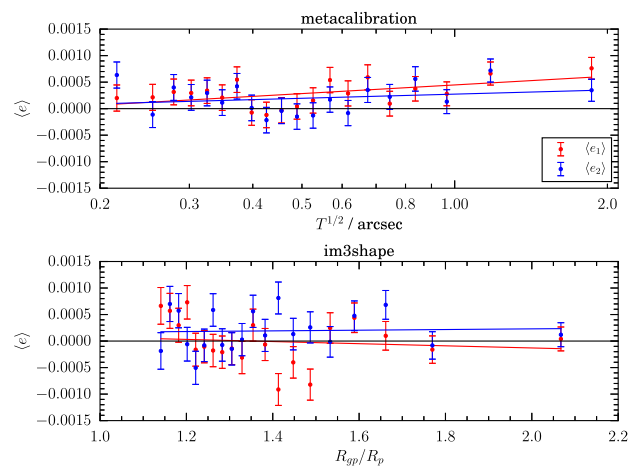
Figure 23. The mean galaxy shear as a function of the galaxy size (METACALIBRATION top, on a logarithmic scale, and IM3SHAPE bottom). The solid lines are a linear best fit to the data points.

the presence of B modes as a null test.[8] In Fig. 24 we show tomographic B-mode measurements using the redshift bins used for cosmology measurements in Troxel et al. (2017) and DES Collaboration (2017). They are computed using a pseudo-C_ℓ estimator (Hikage et al. 2011). The displayed χ^2 values are for individual bins; the total χ^2 values, which also account for the correlations between bins, are 99.8 for METACALIBRATION and 90.8 for IM3SHAPE, which for 90 data points indicates no evidence for B-modes.

6.5 Summary of systematics tests

There are two additive systematics, a PSF-related term and mean shear, which should each be subtracted, marginalized over, or demonstrated to be subdominant in precision analyses. They are described in Sections 3.3 and 7.1, respectively.

There is also a residual uncertainty in the overall multiplicative calibration of the two catalogues, which should be marginalized over. This is described in Section 7.6.

We have found no tests that imply any further systematic errors are present at a level significant for our cosmological analyses.

7 USING THE SHEAR CATALOGUES

7.1 Mean shear

Both catalogues show a non-zero mean ellipticity over the entire Y1 survey, with a value $e_{1,2} = (3.5, 2.8) \times 10^{-4}$ for METACALIBRATION and $e_{1,2} = (0.4, 2.9) \times 10^{-4}$ for IM3SHAPE. This is marginally too large to be the mean of cosmic shear over the field: in log-normal simulations we find a standard deviation of the mean $e_{1,2} \sim 1 \times 10^{-4}$ over our region. An added constant shear will appear as a constant offset in correlation function measurements, so this signal should either be subtracted or marginalized over in cosmological parameter estimation.

The origin of this mean shear is not known definitively, and may be the combination of several effects. Charge self-interaction effects in the DECam CCDs on star and galaxy profiles are expected

---

[8]Higher order lensing effects and PSF leakage can both generate B modes, but not at a level detectable here.
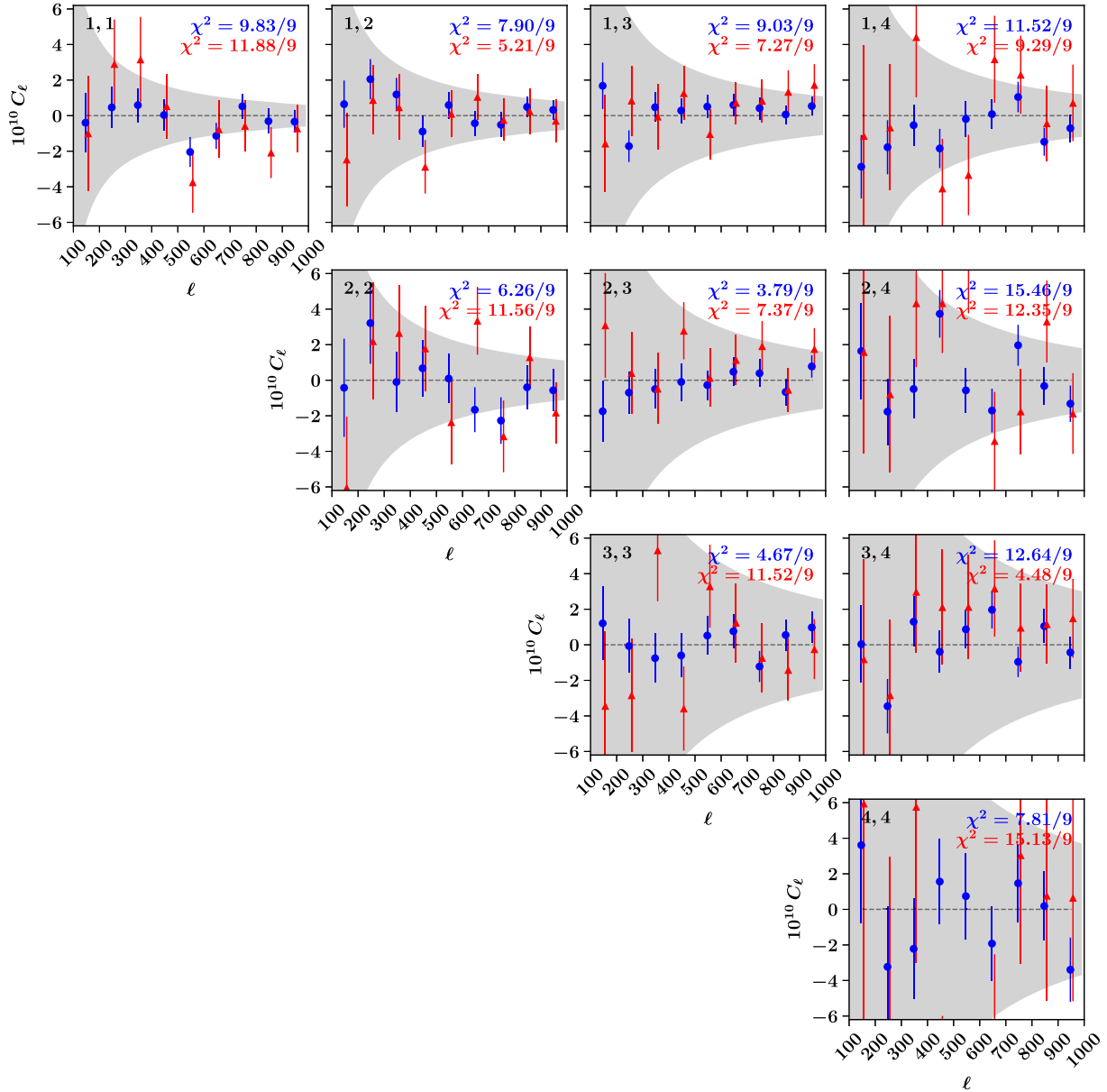
Figure 24. The measured B mode in METACALIBRATION (blue circles) and IM3SHAPE (red triangles), and the corresponding detection χ^2 values. The measurements use the tomographic bins 1–4 as used in Troxel et al. (2017), and the auto- and cross-correlations between them are shown. The value is expected to be close to zero in the absence of systematics. Error bars were calculated from a set of lognormal simulations matching the DES-Y1 survey geometry and redshift distributions. The grey b and show ± the E-mode signal in a fiducial cosmology.

to cause mean shears in the e_1 direction that are of the order of a few times 10^{-4} (cf. table 1 of Gruen et al. 2015). The PSF correlations in Fig. 19 are also expected to contribute a similar order of magnitude, but our model of the PSF model errors does not entirely describe this mean shear (Troxel et al. 2017).

7.2 Catalogue flags

Each catalogue uses its own flagging scheme to determine which galaxies can safely be used in science applications.

IM3SHAPE uses a similar flagging scheme as in J16, based on a small number of 'error flags' that remove extreme objects, and a larger number of 'info flags' that remove the tails of histograms in various quantities. They are combined into a single

FLAGS_SELECT=0 value in our final catalogues. The flags are applied when computing the calibration scheme, so they should always be used identically in precision applications, by requiring:

$$\text{FLAGS\_SELECT} = 0. \tag{26}$$

The flag values are described in Appendix E. The main changes we have made since J16 are reducing our minimum S/N from 15 to 12, and our minimum R_{gp}/R_p from 1.15 to 1.13, reflecting our improved calibration simulations for small faint objects.

The METACALIBRATION catalogue can be adapted to new data cuts, as described below in Section 7.4. As a default cut, which is incorporated into the FLAGS_SELECT column, we use and recom-
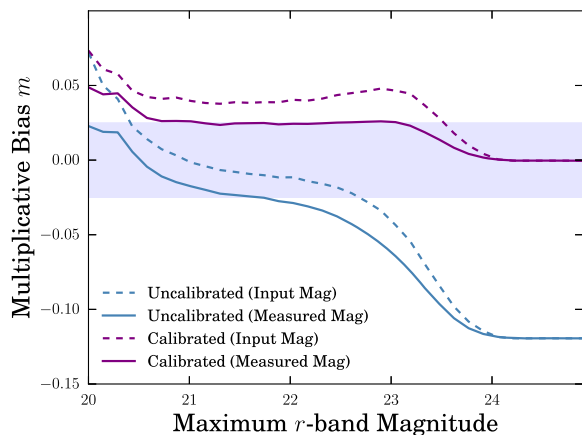
Figure 25. Multiplicative bias for IM3SHAPE, measured from the HOOPOE image simulation. Solid lines show the measured bias after imposing a maximum *r*-band magnitude, using the measured values from the SEX-TRACTOR run on the simulation. Dashed lines show the same, but defining the cut using the input magnitudes. Purple curves use the fiducial calibration scheme described in Section 5.2, and blue curves are uncalibrated. The shaded region shows the 2.5 per cent range that is our final IM3SHAPE calibration uncertainty. This illustrates the danger of selection biases when cutting on any observable which correlates with ellipticity, as magnitude does.

mend:

$$S/N > 10$$
$$T/T_{\mathrm{PSF}} > 0.5 \tag{27}$$

7.3 Applying the IM3SHAPE calibration

The IM3SHAPE calibration yields *m* and *c* values for each object, but because they include corrections for selection biases these values are only correct when applied to the specific default IM3SHAPE cuts. Further cuts can induce biases due to noise that correlates between ellipticity and other quantities. We have verified in Section 5.3.2 that the specific split into tomographic bins used in concurrent DES papers does not induce a significant bias, but this cannot be assumed for any other binnings. An example of a cut that does induce significant bias is shown in Fig. 25, which illustrates that imposing an upper magnitude limit can induce biases of 2–6 per cent, depending on the limit.

The IM3SHAPE calibration is applied in the same manner as it was in J16. The estimator for the mean shear on an ensemble of galaxies is

$$\langle \gamma_a \rangle = \frac{\sum_i w_i (e_{a,i} - c_{a,i})}{\sum_i w_i (1 + m_i)}, \tag{28}$$

where $a = 1, 2$ and *i* sums over all objects. For a shear two-point estimator, the additive *c* correction should first be applied, then the galaxy pairs rotated to the tangential and cross directions e^+ and $e^\times$, and the weights and multiplicative corrections applied to these rotated values:

$$\xi_\pm = \frac{\sum_i \sum_j w_i w_j (e_i^+ e_j^+ \pm e_i^\times e_j^\times)}{\sum_i \sum_j w_i w_j (1 + m_i)(1 + m_j)}, \tag{29}$$

where the sums run over (i, j) pairs separated by angle θ.

7.4 Applying the METACALIBRATION calibration

To calibrate the METACALIBRATION catalogues we make use of the five different sets of measurements that the code makes on each object: on the original image, and on versions positively and negatively sheared in the e_1 and e_2 directions. We can use these measurements to calibrate bias in both the shape measurement for each object, and any selection biases. The metacalibration process can only calibrate selection biases when cuts are made on quantities which have been measured by the METACALIBRATION estimator, so that equation (17) can be used to calculate corrections. These include, but are not limited to, galaxy and PSF sizes and ellipticities, S/N, and fluxes.

As an example of the process, one should use this calculation to estimate the mean shear under some selection:

(i) For a given selection criterion *S*, and for each shear component γ_1 and γ_2 determine three subsets of the catalogue:

S_0- by applying *S* to the column measured on the original image,
S_+- by applying *S* to the column measured after positive shear in component *i*,
S_-- by applying *S* to the column measured after negative shear in component *i*.

(ii) For each pair of shear components *i*, *j*, compute $R_{\gamma_{ij}}$, the average of column R_{ij} over galaxies in S_0

(iii) Compute $R_{s_i} = (\langle e_i \rangle_{S_+} - \langle e_i \rangle_{S_-})/\Delta\gamma$, where the e_i columns are the ones measured on the original image, and the averages are taken over the subsets in the subscripts. For DES Y1 we used $\Delta\gamma = 0.01$.

(iv) The complete response for the ensemble is $R_{ij} = R_{\gamma_{ij}} + \delta_{ij} R_{s_i}$.

(v) The best estimate for the mean shear is $\gamma_i = R_{ij}^{-1} \langle e_j \rangle_{S_0}$

The process for correcting a two-point estimator in the same way is described in SH17. For convenience, the default FLAGS_SELECT column has four additional sheared versions, FLAGS_SELECT_X, where X is in {1p, 1m, 2p, 2m}, representing the component and direction of the sheared version of the flag.

To enable bias correction of samples selected by photometric redshift, we have applied our photo-*z* estimators to the flux measured for each galaxy by METACALIBRATION both before and after the METACALIBRATION shears are applied (there are four additional catalogues, for $\pm \delta e_{1,2}$). Given a galaxy selection, if the mean of the shears is to be used, for example in the null tests described in Section 6, the correction factors in Section 4 must be applied. The calibration factor that must be applied when constructing two-point statistics is described in SH17. For higher order statistics an equivalent calibration should be derived. The selection biases in mean shear for the DES redshift bins range from 1.1 to 2.5 per cent.

Note that the correction factors applied to each METACALIBRATION object are large, because the model used is so simple, so neglecting them is unlikely to be a good approximation in any context.

7.5 Number density

Values of the (effective) number density and shape variance for three definitions for the two catalogues are shown in Table 5. The *raw* value is simply the total number of selected objects per unit area.

The variance σ_γ^2 of the estimated shear in a catalogue quantifies its overall constraining power. This quantity is generally split into $\sigma_\gamma^2 \equiv \sigma_e^2/n_{\mathrm{eff}}$, where σ_e^2 is a shape variance and n_{eff} a number density. Any

Table 5. Number density values and noise per component using various definitions as described in the text for the two catalogues.

Catalogue	Definition	Number/arcmin^2	σ_e
METACALIBRATION	Raw	6.38	
	Chang-13	5.96	0.27
	Heymans-12	6.38	0.28
IM3SHAPE	Raw	4.02	
	Chang-13	3.16	0.25
	Heymans-12	3.72	0.28

Table 6. Multiplicative bias budget for METACALIBRATION. For the effect of contributions that are correlated between redshift bins on tomographic analyses, see Appendix D.

Effect	Bin correlation	Mean (10^{-2})	Gaussian σ_m (10^{-2})
Stellar contamination	Yes	0.0	0.2
PSF size bias	Yes	0.0	0.3
Neighbour bias	Yes	1.2	1.2
Total		1.2	1.3

pair of definitions of these two quantities that yield the correct σ_γ^2 may be used as a metric to quantify the constraining power.

The definition described in Chang et al. (2013) is given by

$$n_{\mathrm{eff}}^{\mathrm{C13}} = \frac{1}{A} \sum \frac{\sigma_{\mathrm{sh}}^2}{\sigma_{\mathrm{sh}}^2 + \sigma_{m,i}^2}, \tag{30}$$

where A is the surveyed sky area. For METACALIBRATION the measurement noise $\sigma_{m,i}^2$ is derived from the estimated measurement covariance matrix, accounting for the response term, and the intrinsic shape noise σ_{sh}^2 then derived from this and the total observed variance (the denominator). For IM3SHAPE the shape noise is estimated from high signal-to-noise objects where measurement noise is minimal, and the measurement noise derived from this and the total variance.

The total shape variance σ_e^2 for one galaxy is the term $\sigma_{\mathrm{sh}}^2 + \sigma_{m,i}^2$.

The definition in Heymans et al. (2012) is useful here for comparison to other surveys:

$$n_{\mathrm{eff}}^{\mathrm{H12}} = \frac{1}{A} \frac{\left(\sum w_i\right)^2}{\sum w_i^2}. \tag{31}$$

Since we use unit weights for METACALIBRATION this is the same as the raw value for that catalogue.

7.6 Systematic error budget

Additive errors from the PSF, including the αe_{PSF} PSF leakage term, have been discussed in Section 6.2. In the following, we will describe the budget of multiplicative systematic errors m to be used with both shape catalogues. In general, where we have an untreated systematic then we add the full width of its possible range to the prior on m. Where we have a systematic that is treated but we believe the treatment to be imperfect, we add 50 per cent of the width to the prior.

We do not have a hard requirement on the multiplicative bias, since any uncertainty can be marginalized over at the parameter estimation stage, but at about 2 per cent uncertainty the associated error is comparable to the statistical uncertainty in the data.

7.6.1 METACALIBRATION

The dominant contribution to the systematic calibration uncertainty of the METACALIBRATION shear catalogue is the effect of overlapping objects.

Additional multiplicative bias contributions arise from two effects related to the slight size bias of our PSF models, described in detail in Sections 4.5 and 4.5.1. These are strongly subdominant to the neighbour bias and its uncertainty, especially when added in quadrature, which is appropriate since the effects are a priori uncorrelated. An overview is shown in Table 6, which results in a total Gaussian prior on the multiplicative bias with centre $m = 0.012$

and 1σ width 0.013. We note that all of the effects contributing to METACALIBRATION multiplicative bias are potentially highly correlated between source redshift bins in a tomographic analysis, a fact that needs to be accounted for (see Appendix D for details).

7.6.2 IM3SHAPE

As in DES-SV (see Jarvis et al. 2016, their section 7.3.2), we calibrate the IM3SHAPE catalogue using image simulations. For DES Y1, however, we have developed a new independent pipeline for generating image simulations, which includes several improvements intended to mimic the properties of actual Y1 data as closely as possible (see Table 2 and Samuroff et al. 2018). Unlike SV, where the multiplicative bias uncertainty was estimated by the (dis)agreement of our two pipelines on simulations, our systematics budget for IM3SHAPE is now set by quantifiable residual uncertainties in the statistics and methodology of the simulation-based calibration.

A main part of this uncertainty is due to the effect of detected and undetected neighbours on multiplicative bias. Comparison of IM3SHAPE runs on identical sets of simulations with and without neighbouring galaxies (Samuroff et al. 2018) (see their fig. 16) has shown a mean shift in calibration corresponding to $\Delta m = -0.034$ – mean shears measured in simulations with neighbours are about 3 per cent larger than for a sample of fully isolated galaxies. While our simulation-based calibration is a bona fide correction of this effect that should capture its dominant influence on shape measurement, some aspects of the effect in real data might not be captured in the simulations. Among these are the relative alignment of physical neighbours and coherently sheared projected neighbours (both of which, however, influence the distribution of relative alignments only slightly), the influence of completely blended galaxies (which are rare in DES data), or the clustering and coherent alignment of undetected background galaxies (which are, however, altogether a subdominant contribution to neighbour-related bias in IM3SHAPE as shown in Samuroff et al. 2018). We therefore assume half of the neighbour-induced shift in our calibration as an uncertainty, giving $\sigma_m = 0.017$, which is conservative given the degree of realism present in the simulations.

Additional systematic uncertainties in the simulation-based calibration are due to

(i) assignment of cut-out sizes in the MEDS file – While stamp size in the real data is based on measurements of a source's size and ellipticity performed on the coadd using SEXTRACTOR, in the bulk of the simulations the code mistakenly truncated each simulated galaxy's image at the bounds of a postage stamp of the original source whose position it was taking. Larger or highly elliptical galaxies in our simulations are therefore often assigned smaller boxes than they would in the data. When we remove galaxies from the simulations that are in an incorrectly sized box, the population of

galaxies used in deriving the calibration significantly changes. We were unable to devise a cut based on the true input properties of the simulated galaxies that did not significantly alter the ellipticity and size distributions. Reweighting was found to be unreliable (since the cut leaves very few large elliptical galaxies to upweight) and not robust to binning in S/N and R_{gp}/R_p. Re-running the calibration on a small subset of the data with this problem fixed, we find a maximum change in multiplicative bias of 0.025.

We conservatively assume a top-hat prior of $|m| < 0.025$ per redshift bin, corresponding to a Gaussian $\sigma_m = 0.014$. While this is a non-negligible contribution to our overall error budget, rerunning the full simulation with box sizes assigned according to properties measured in the stack, as is done in the data, would require a large computational overhead and represents a non-trivial restructuring of the simulation pipeline that we defer to future work.

(ii) removal of bad objects from the COSMOS galaxy sample – We have manually identified galaxies among the COSMOS library that show issues potentially affecting multiplicative bias calibration (see Appendix A). The change in calibration when removing flagged galaxies is at most 0.009 among the top-hat redshift bins. Despite these efforts, the choice of which galaxies to remove remains somewhat subjective, and the change in the galaxy properties of the sample that ends up being used in the simulations could cause a small systematic difference of our calibration sample from the galaxies present in the real data. We therefore assume half of the observed shift, or 0.005, as a systematic uncertainty.

(iii) variation of morphology as a function of redshift – Our calibration is described by a function of signal-to-noise ratio and size, which are the two most important parameters affecting noise and selection biases, and performed separately for galaxies better fit by bulge- and disc-type Sérsic profiles. Noise bias does, however, depend on additional galaxy properties whose distributions at given signal-to-noise ratio and size vary as a function of redshift. When we apply the calibration derived from the full galaxy sample to a redshift bin in our simulations, we therefore find deviations from zero bias, which are at most at the level of 0.01. These residual biases are robust to all of the choices which enter the calibration scheme (interpolation, binning, etc.). Since lensing analyses virtually always employ some implicit or explicit redshift-dependent re-weighting of sources, we assume an additional systematic uncertainty of this size in each redshift bin.

Summing in quadrature, these effects amount to a Gaussian systematic uncertainty of $\sigma_m = 0.018$.

The volume of our simulations is large but finite, leading to a statistical uncertainty on mean m of $\sigma_m = 0.002$.

In addition, IM3SHAPE suffers biases from the mean size residual in our PSF models. To assess the impact of error in the interpolated PSF kernel at source positions, we run IM3SHAPE on the high S/N simulations described in Section 4.5.1. These images consisted of analytic profiles under constant shear $\mathbf{g} = (0.01, 0.00)$, and convolved with highly elliptical Moffat PSFs. Using these simple simulations we compute a single-number mean bias m. Given the lack of variance in g, and the low noise in these images the statistical error on these measurements can safely assumed to be negligible at $\mathcal{O}(10^{-4})$. Comparing the results from the reference simulations (no PSF size bias) with a set of images with a mean dilation $\langle \Delta T_{PSF}/T \rangle \sim 8.3 \times 10^{-4}$ we find a change in the mean multiplicative bias of $\Delta m = 0.006$. While these simulations likely capture the dominant part of the effect, realistic galaxy morphology might change the result at a second order level. Adopting a conservative approach, we scale this observed change by a factor

Table 7. Multiplicative bias budget for IM3SHAPE. The calibration systematic error includes the effects of cut-out size, removal of bad objects from the COSMOS sample, and variation of morphology besides size as a function of redshift. For the effect of contributions that are correlated between redshift bins on tomographic analyses, see Appendix D.

Effect	Bin correlation	Mean [10^{-2}]	Gaussian σ [10^{-2}]
Stellar contamination	Yes	0.0	0.1
PSF size bias	Yes	0.0	0.4
Neighbour bias	Yes	0.0	1.7
Calibration statistical	Yes	0.0	0.2
Calibration systematic	No	0.0	1.8
Total		0.0	2.5

of 1.5 before incorporating it into our m prior. After conversion to Gaussian width, maintaining variance, the total impact is $\sigma_m = 0.005$. Note that we find no change in additive biases between the two simulations.

Contamination of our IM3SHAPE source sample with point sources is a negligible effect at the strict cuts we have applied to the catalogue, which we include in the error budget at an estimated level below one per-mille.

Adding these effects in quadrature, as shown in an overview in Table 7, we arrive at a total Gaussian prior on the multiplicative bias with centre $m = 0.0$ and 1σ width 0.025. Some of the effects contributing to the multiplicative bias are correlated between source redshift bins and estimated in a way that requires us to account for this fact in a tomographic analysis (see Appendix D for details).

8 SUMMARY AND DISCUSSION

We have presented two independent catalogues of shape measurements of galaxies imaged in Year One of the Dark Energy Survey, covering 1500 deg^2 of the Southern sky and containing 34.8 million (for METACALIBRATION) and 21.9 million (for IM3SHAPE) objects. They have passed a battery of tests that demonstrate that, when appropriately used with calibration and error models, they are suitable for weak lensing science. In companion papers we also demonstrate that these catalogues lead to consistent cosmological constraints: in Troxel et al. (2017) we study constraints from cosmic shear, in Prat et al. (2017) we examine galaxy–galaxy lensing, and in DES Collaboration (2017) we study both in conjunction with galaxy density correlation functions.

This work is the first application of the metacalibration method to real data, and demonstrates its significant power in the face of noise and model biases, and especially for its approach to dealing with the pernicious issue of selection biases. This work also makes use of the most sophisticated image simulations currently used for lensing noise and model bias calibration, which account for a wide range of systematic effects that would otherwise produce a significantly biased IM3SHAPE catalogue. We emphasize the importance of carefully ensuring that simulations match the data in as many ways as possible, including PSF patterns, masks, weights, and processing selections.

Since the analysis of our science verification SV data in Jarvis et al. (2016) we have made the following improvements to our shape pipelines, in addition to the improvements in data reduction described in Drlica-Wagner et al. (2018):

(i) Implemented the metacalibration technique, to incorporate internal calibration of measurement and selection biases, into the METACALIBRATION pipeline.

(ii) Included neighbours, sub-detection objects, stars, masks, realistic PSFs, and multiple exposures, in our calibration simulations for the IM3SHAPE pipeline.

(iii) Explored the effects of blending on our results.

(iv) Identified that PSF-associated errors arise almost solely from mis-estimation of the PSF itself.

(v) Enumerated a full list of error sources contributing to our final uncertainty.

As in the SV analysis, having two independent methods for shear estimation has provided us with significantly greater confidence in the robustness of the catalogue calibrations.

Like all weak lensing catalogues, the DES Y1 results come with an uncertainty on overall calibration in the form of a multiplicative bias m. Correctly and conservatively determining priors on this quantity is a vital part of characterising a lensing catalogue, and in this case we obtain $\sigma_m \sim 1.2 \times 10^{-2}$ for METACALIBRATION and $\sigma_m \sim 2.5 \times 10^{-2}$ for IM3SHAPE. These values are small enough that this systematic is subdominant in cosmic shear cosmology parameter estimation. An additional correction is required due partly to mis-estimation of the PSF, which leads to correlation of the inferred shear with the PSF shape and a correctable residual additive bias in the catalogues.

The data presented here comprise only 20 per cent of the full Dark Energy Survey, and work to analyse the subsequent 2 yr of data has already begun. To fully exploit that upcoming opportunity, the methods described here must be refined and improved in a number of major ways. We plan to further extend our calibration simulations to more precisely mimic the processes applied to real data. We will continue to improve and adapt our shape measurement algorithms, including incorporating new methods like BFD and applying novel calibration techniques like metacalibration to existing methods like IM3SHAPE using multiple bands. We are also in the process of implementing a new PSF measurement pipeline to reduce the significant PSF model residuals found in our Y1 catalogues.

The catalogues presented in this paper will be made publicly available following publication, at the URL https://des.ncsa.illinois.edu/releases.

REFERENCES

Aihara H. et al., 2018, PASJ, 70, S8

Albrecht A. et al., 2006, preprint (arXiv:astro-ph/0609591)

Amon A. et al., 2018, MNRAS, 477, 4285

Antilogus P., Astier P., Doherty P., Guyonnet A., Regnault N., 2014, J. Instrum., 9, C3048

Bartelmann M., Schneider P., 2001, Phys. Rep., 340, 291

Bernstein G. M., Armstrong R., 2014, MNRAS, 438, 1880

Bernstein G. M., Jarvis M., 2002, AJ, 123, 583

Bertin E., 2006, in Gabriel C., Arviset C., Ponz D., Enrique S., eds, ASP Conf. Ser. Vol. 351, Astronomical Data Analysis Software and Systems XV. Astron. Soc. Pac., San Francisco, p. 112

Bertin E., 2010, Astrophysics Source Code Library, record ascl:1010.063

Bertin E., 2011, in Evans I. N., Accomazzi A., Mink D. J., Rots A. H., eds, ASP Conf. Ser. Vol. 442, Astronomical Data Analysis Software and Systems XX. Astron. Soc. Pac., San Francisco, p. 435

Bertin E., Arnouts S., 1996, A&AS, 117, 393

Bridle S. et al., 2010, MNRAS, 405, 2044

Britton D. et al., 2009, Phil. Trans. R. Soc. A, 367, 2447

Chang C. et al., 2013, MNRAS, 434, 2121

DES Collaboration, 2018, Phys. Rev. D, 98, 043526

Diehl H. T. et al., 2014, in Peck A. B., Benn C. R., Seaman R. L., eds, Proc. SPIE Conf. Ser. Vol. 9149, Observatory Operations: Strategies, Processes, and Systems V. SPIE, Bellingham, p. 91490V

Drlica-Wagner A. et al., 2018, ApJS, 235, 33

Fenech Conti I., Herbonnet R., Hoekstra H., Merten J., Miller L., Viola M., 2017, MNRAS, 467, 1627

Flaugher B. et al., 2015, AJ, 150, 150

Gruen D., Bernstein G. M., Jarvis M., Rowe B., Vikram V., Plazas A. A., Seitz S., 2015, J. Instrum., 10, C05032

Guyonnet A., Astier P., Antilogus P., Regnault N., Doherty P., 2015, A&A, 575, A41

Heymans C. et al., 2006, MNRAS, 368, 1323

Heymans C. et al., 2012, MNRAS, 427, 146

Hikage C., Takada M., Hamana T., Spergel D., 2011, MNRAS, 412, 65

Hildebrandt H. et al., 2016, MNRAS, 463, 635

Hildebrandt H. et al., 2017, MNRAS, 465, 1454

Hirata C., Seljak U., 2003, MNRAS, 343, 459

Hirata C. M. et al., 2004, MNRAS, 353, 529

Hoekstra H., Herbonnet R., Muzzin A., Babul A., Mahdavi A., Viola M., Cacciato M., 2015, MNRAS, 449, 685

Hoekstra H., Viola M., Herbonnet R., 2017, MNRAS, 468, 3295

Hoyle B. et al., 2018, MNRAS, 478, 592

Huff E., Mandelbaum R., 2017, preprint (arXiv:1702.02600)

Huff E. M., Eifler T., Hirata C. M., Mandelbaum R., Schlegel D., Seljak U., 2014, MNRAS, 440, 1322

Jarvis M., Jain B., Bernstein G., Dolney D., 2006, ApJ, 644, 71

Jarvis M. et al., 2016, MNRAS, 460, 2245

Jee M. J., Tyson J. A., Schneider M. D., Wittman D., Schmidt S., Hilbert S., 2013, ApJ, 765, 74

Jouvel S. et al., 2009, A&A, 504, 359

Kacprzak T., Zuntz J., Rowe B., Bridle S., Refregier A., Amara A., Voigt L., Hirsch M., 2012, MNRAS, 427, 2711

Kaiser N., Squires G., Broadhurst T., 1995, ApJ, 449, 460

Kitching T. D. et al., 2012, MNRAS, 423, 3163

Koekemoer A. M. et al., 2007, ApJS, 172, 196

Lin H. et al., 2012, ApJ, 761, 15

Mandelbaum R. et al., 2005, MNRAS, 361, 1287

Mandelbaum R. et al., 2015, MNRAS, 450, 2963

Massey R. et al., 2007, MNRAS, 376, 13

Miller L., Kitching T. D., Heymans C., Heavens A. F., van Waerbeke L., 2007, MNRAS, 382, 315

Moffat A. F. J., 1969, A&A, 3, 455

Neilsen E. H., Jr., Bernstein G., Gruendl R., Kent S., 2016, Technical report, Limiting Magnitude, τ, t_{eff}, and Image Quality in DESY Year 1. Fermi National Laboratory

Paulin-Henriksson S., Amara A., Voigt L., Refregier A., Bridle S. L., 2008, A&A, 484, 67

Plazas A. A., Bernstein G. M., Sheldon E. S., 2014a, J. Instrum., 9, C04001

Plazas A. A., Bernstein G. M., Sheldon E. S., 2014b, PASP, 126, 750

Prat J. et al., 2017, Phys. Rev. D, 98, 042005

Refregier A., 2003, MNRAS, 338, 35

Refregier A., Kacprzak T., Amara A., Bridle S., Rowe B., 2012, MNRAS, 425, 1951

Roodman A., Reil K., Davis C., 2014, in Stepp L. M., Gilmozzi R., Hall H. J., eds, Proc. SPIE Conf. Ser. Vol. 9145, Ground-based and Airborne Telescopes V. SPIE, Bellingham, p. 914516

Rowe B., 2010, MNRAS, 404, 350

Rowe B. T. P. et al., 2015, Astron. Comput., 10, 121

Rozo E. et al., 2016, MNRAS, 461, 1431

Samuroff S. et al., 2018, MNRAS, 475, 4524

Schrabback T. et al., 2007, A&A, 468, 823

Scoville N. et al., 2007, ApJS, 172, 1

Seitz C., Schneider P., 1997, A&A, 318, 687

Sheldon E., 2015, Astrophysics Source Code Library, record ascl:1508.008

Sheldon E. S., Huff E. M., 2017, ApJ, 841, 24

Skrutskie M. F. et al., 2006, AJ, 131, 1163

Soumagnac M. T. et al., 2015, MNRAS, 450, 666

Troxel M. A. et al., 2017, Phys. Rev. D, 98, 043528

Van Waerbeke L., Mellier Y., Hoekstra H., 2005, A&A, 429, 75

Zacharias N., Finch C. T., Girard T. M., Henden A., Bartlett J. L., Monet D. G., Zacharias M. I., 2013, AJ, 145, 44

Zuntz J., Kacprzak T., Voigt L., Hirsch M., Rowe B., Bridle S., 2013, MNRAS, 434, 1604

APPENDIX A: THE COSMOS EYEBALL PROJECT

It was noted after they had been run that the simulations described in Section 5.2 contained a small number of obvious artefacts, originating from defects in the input COSMOS profiles. These included deblending failures, and objects with diffuse light profiles truncated at the edges of the postage stamp. Two such objects are shown in Fig. A1. To assess the level to which these objects affect shape measurements on the simulations we initiated a small-scale crowd-sourcing project within the scientific community of the Dark Energy Survey. Our specific aim here was to compile a list of COSMOS galaxies in our input catalogues that are qualitatively 'bad', and so should be excluded from our simulations.
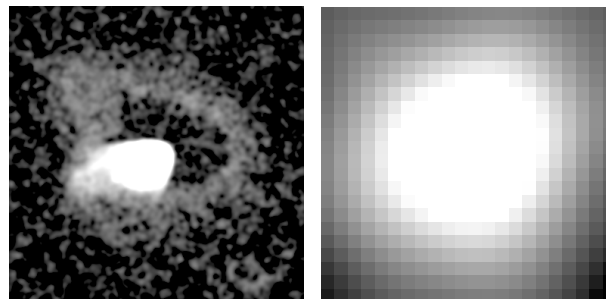
Figure A1. Examples of profiles flagged as 'bad' by the COSMOS classification exercise described in the text. The two galaxies shown here were classed as *artefact* (left) and *box too small* (right). For a breakdown of the number in each category see Table A1.
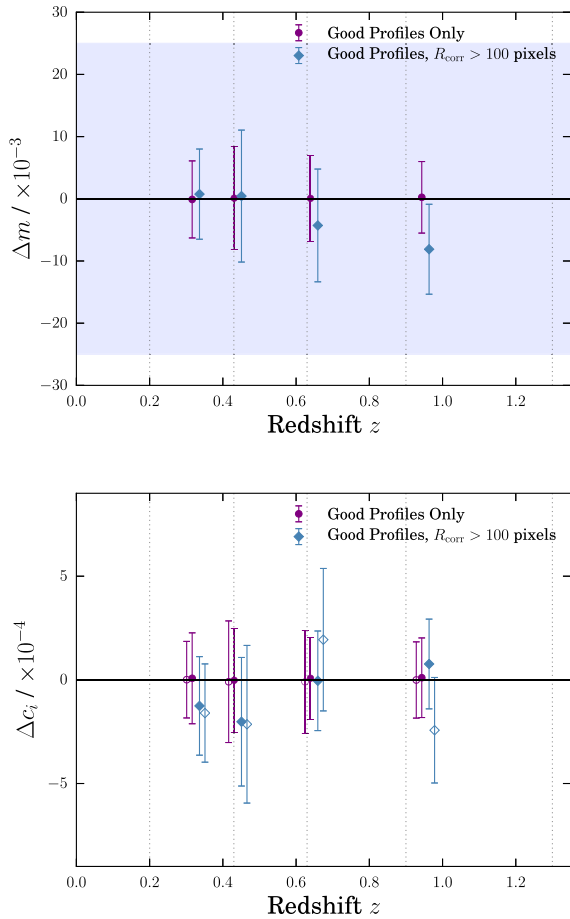
Figure A2. Change in the multiplicative bias (top) and additive bias (bottom) after removal of bad COSMOS profiles, relative to the value derived using all galaxies. In the lower panel the filled markers show the c_1 component and the open ones show c_2.

The exercise was set up as follows. Each deconvolved COSMOS galaxy was reconvolved with a small nominal PSF and rendered into a postage stamp image at *HST* pixel resolution with no additional noise. The images were compiled in random order, and via a simple web interface users were assigned batches of ~100 images. Galaxies were assigned to the categories shown in Table A1.

To test the impact of the aberrant COSMOS profiles on the IM3SHAPE calibrations we fit for multiplicative and additive bias in the HOOPOE dataset three times with different selection criteria: (a) IM3SHAPE quality cuts only; (b) removing any objects classed as 'bad' for any reason; and (c) the same as (b), but additionally cutting any galaxies that fall within a circular aperture of 100 pixels around each flagged COSMOS profile. The results, in four DES Y1-like tomographic bins, are shown in Fig. A2.

The straightforward cut (b) induces a shift Δm that is comfortably within the level of statistical error of the fit. The second test suggests the corrupted profile may induce a small neighbour bias on surrounding profiles, which manifests as a modulation in *m*. It is worth pointing out that some of the categories listed in Table A1 may be benign. Off-centred galaxies and those with neighbours, for example, should not cause a problem, since we re-run SEXTRACTOR object detection and deblending on the simulations. Our final cut on the simulation rejects instances of COSMOS profiles categorized under 'artefact', 'box too small', or 'galaxy missing'. We test that additionally cutting the other categories does not induce a statisti-

Table A1. The number of input galaxies in the Y1 DES image simulations presented in Chapter 3 falling under each category in the profile inspection exercise described. The first three columns show (left to right) the total number of COSMOS galaxies in each category from the full source catalogue from which the simulation draws profiles, the number of simulated galaxies affected, and the corresponding number of COSMOS profiles (note that the second and third columns are not identical since each COSMOS profile is drawn into multiple positions).

Category	COSMOS profiles	Galaxies in HOOPOE	COSMOS profiles in HOOPOE
Total	87624	17.97 M	27 612
Good	76707	16.93 M	25 878
Box too small	3743	0.16 M	424
Artefact	1024	0.35 M	410
Two galaxies	542	0.40 M	375
Galaxy missing	4212	0.08 M	354
Off centre	915	0.05 M	171
Other	481	0.10 M	127

cally significant change in bias. Based on the results in Fig. A2, we also incorporate a Gaussian component of width $\sigma_m = 0.005$ in the residual *m* prior for IM3SHAPE.

APPENDIX B: SENSITIVITY OF HOOPOE SIMULATIONS TO OBSERVABLE DISTRIBUTIONS

Though our calibration appears to pass the internal tests presented in Section 5.3, it is still possible that residual biases could arise due to differences with the data seen in Section 5.2.5. The most notable differences are in flux and R_{gp}/R_p. The raw distributions of R_{gp}/R_p and flux are shown by the solid lines in Fig. B1, with the parent DES data shown by the shaded histograms.

We assess the importance of these differences by reweighting the HOOPOE simulations to match the data. In the case of R_{gp}/R_p we simply divide galaxies into bins of size and assign a uniform weight to each bin, such that the simulated distribution $p(R_{gp}/R_p)$ matches the data. In the second case we carry out the same procedure for galaxy flux. This time, however, an independent set of weights is computed for bulge and disc galaxies, such that they each match the corresponding sub-populations of the data. The reweighted distributions are shown by the dashed lines in Fig. B1.

As pointed out by Fenech Conti et al. (2017), who carried out a similar test for KiDS, reweighting can be problematic if the quantities in question are covariant with ellipticity. In such cases reweighting to match a 1D projected distribution $p(q)$ may be inadequate to correct (or even worsen) differences in the 2D joint distribution $p(q, e)$. In each case we check both the 2D distributions (not shown here) and the 1D $p(e)$ histograms (shown in the right-hand panels of Fig. B1). Neither reweighting operation is found to produce such spurious differences.

Finally, galaxies are divided into four Y1-like tomographic bins, as before, the fiducial calibration is applied, and the residual *m* is calculated in each bin. The results are shown in Fig. B2. The maximum change under reweighting Δm in both cases is $\mathcal{O}(10^{-3})$. This is not found to have a coherent direction across *z* bins, and is well within both the statistical error margin (the blue shaded boxes) and the 1σ width of our prior (the dashed horizontal lines).

Reweighted for Flux

Reweighted for R_{gp}/R_p
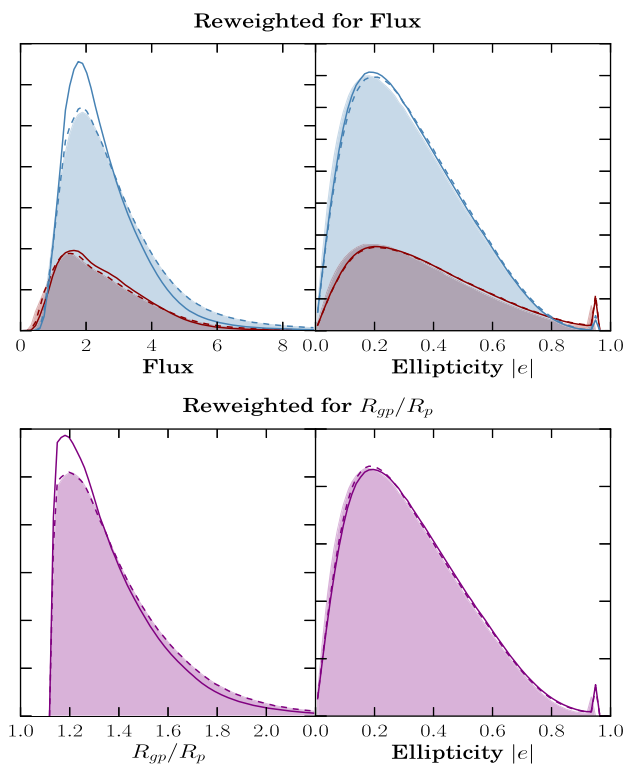
Figure B1. Histograms of flux (upper left), size (lower left), and ellipticity (upper/lower right) in the data (shaded region) and simulations used for IM3SHAPE calibration before (solid) and after (dashed) objects are reweighted to match the flux (top) and size (bottom) distributions in the data. In the upper panel we show bulge and disc galaxies separately in red and blue respectively.
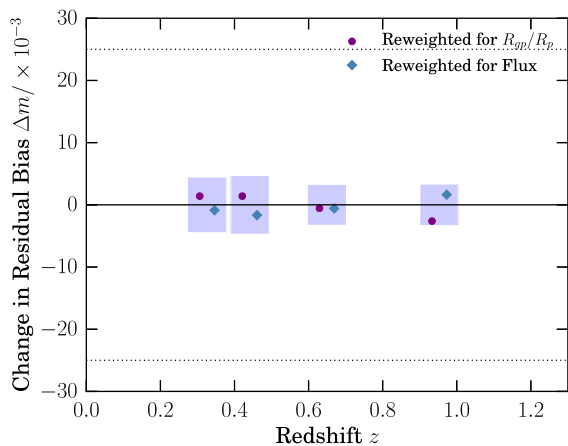
Figure B2. Change in the residual IM3SHAPE bias resulting from reweighting the simulations prior to calibration, shown in the four tomographic bins used in the DES Y1 shear 2pt analysis. The purple circles show the result when reweighting to compensate for the excess of small galaxies shown in the centre-right panel of Fig. 12, while the blue diamonds are reweighted for bulge/disc flux. The blue bands mark the 1σ statistical error on m, while the horizontal dotted lines are the $\pm 1\sigma$ bounds of the m prior for IM3SHAPE.

APPENDIX C: VALIDATING THE HOOPOE SIMULATIONS

In this appendix we describe a series of exercises to test the level at which features of our HOOPOE simulations which are systematically different from the data affect the multiplicative bias calibration. Any such effects which have a non-vanishing impact must be included in our prior on residual m after calibration.

The first limitation comes from the fact that a finite selection of COSMOS galaxies is used to simulate a much larger sample of DES galaxies. The cache of input profiles, though continuously updated is relatively small, which results in the same COSMOS galaxies appearing repeatedly within particular regions of the simulated images. Such effects could conceivably lead to additive or multiplicative biases, if the frequency of repetition is sufficiently high. To test this we divide the HOOPOE galaxies according to COSMOS identifier. For each unique profile we construct a k–d tree data structure on the coadd pixel grid. This is repeatedly queried to locate the nearest instance of the same COSMOS profile.

We find a mean recurrence scale of $\sim$150 pixels or 40.5 arcsec, though there is a significant asymmetry in the distribution of distances with a heavy tail out to 1000 pixels and higher. The fraction of galaxies with a relatively close self-neighbour is, however, also non-vanishing. We thus perform the following test. HOOPOE galaxies are first assigned to four top-hat redshift bins, as described in Section 5.3.2. In each bin we fit for multiplicative and additive biases (a) using all galaxies and (b) using only galaxies with no instance of the same profile within a radius of 100 pixels. The raw number removed by the cut is relatively small, but it could conceivably favour small round objects. To ensure we are measuring the true impact of self-neighbours, and not a selection effect from the cut devised to remove them, we reweight the surviving galaxies. Weights are assigned based on S/N and R_{gp}/R_p, such that, when applied, the 2D histogram $p(\mathrm{S/N}, R_{gp}/R_p)$ matches the data. We find no significant change in multiplicative nor additive bias in any of the redshift bins ($\Delta m \sim 10^{-4}$, $\Delta c_i \sim 10^{-5}$).

A second limitation concerns the nature of the input COSMOS profiles themselves. The simulations make use of an early release of the deep COSMOS catalogue. Due to masking errors and deblending failures a fraction of this input catalogue is visibly defective. We use an internal crowdsourcing exercise, the details of which can be found in Appendix A, to categorize the COSMOS galaxies into six groups according to their visual characteristics. In the final cut we remove profiles flagged as 'artefacts' or oversized relative to their boxes. In total this removes 0.51M/18M objects from the simulated shape catalogue. Using a similar nearest neighbour search as above, we estimate mean distance to the nearest 'bad' COSMOS profile to be $\sim$90 pixels. We recompute the biases m and c_i under three scenarios: (a) using all galaxies, (b) cutting COSMOS profiles classed as artefacts or oversized and (c) the same as (b), but also cutting galaxies drawn within 100 pixels of a bad COSMOS profile. We find the computed biases are stable to well within 1σ in all apart from the upper redshift bin. Here we lose the bulk of the galaxies removed by this cut, which is perhaps unsurprising given that these objects tend to be small, faint and thus most susceptible to deblending failures. The change in all scenarios is at the level of the 1σ statistical error at $\Delta m \sim 0.005$–0.0075. Though small, this is non-trivial and so we incorporate this uncertainty as a systematic contribution to our m prior (see Section 7.6).

The use of the Y1 detection catalogue to source the positions of simulated galaxies is intended to capture the galaxy clustering patterns across the survey. It does have some drawbacks, chiefly that it omits undetected or strongly blended galaxies (see Section 5.2.4). A second potential limitation is this: not all detections in the Y1 source catalogue correspond to real galaxies. Spurious detections can be produced by CCD chip edges and by image artefacts such as satellite trails and ghosts. These detections are removed prior to shape measurement and do not feature in the final GOLD catalogues, but the raw detection catalogues, which are used as inputs to our simulations, do not provide sufficient information to distinguish real from false detections during runtime.

We tried a simple detection algorithm to flag these features, using boxcar averaged source densities, but this was not found to reliably detect diagonal or curved streaks. The HOOPOE images consequentially include infrequent but visually striking lines of COSMOS galaxies in these locations. To quantify the impact, we implemented a second crowdsourcing exercise, analogous to the one described in Appendix A. We first ran the boxcar detection algorithm on the simulated coadd images, and created visual bookmarks for these detections. Participants were then asked to inspect approximately half of the simulated tiles, each of which was split into 5×5 square patches. Patches in which the detection positions exhibited visible structure were flagged for removal. As before we then divide HOOPOE galaxies into DES-like redshift bins and recompute m and c_i, first including the flagged regions and then excising them. Using all galaxies (no redshift binning) we find a shift $\Delta m = 3.7 \times 10^{-5}$, which is equivalent to less than 2 per cent of the 1σ statistical uncertainty on m. In four redshift bins, and again reweighting to ensure the $p(\text{S/N}, R_{gp}/R_p)$ distribution still matches the data, we measure $m = (-0.0969, -0.1583, -0.1697, -0.2160)$ with the spurious detection lines cut and $m = (-0.0973, -0.1581, -0.1691, -0.2160)$ when they are included. That is, the cut alters m by at most $\Delta m = 0.0007$. Since any systematic shift is subdominant to statistical uncertainty, we do not consider spurious detections further as a source of systematic calibration error.

APPENDIX D: MULTIPLICATIVE BIASES IN TOMOGRAPHIC MEASUREMENTS

The uncertainties σ_m on multiplicative bias m of the METACALIBRATION and IM3SHAPE catalogues given in Section 7.6 are valid for our overall source sample without redshift binning or weighting. The true multiplicative biases present in our catalogues likely vary as a function of redshift. We do not have a reliable model for this variation, so instead must use different multiplicative bias parameters m_i for different bins in tomographic analyses. In this appendix we consider how m values should be statistically correlated between redshift bins. Which choice of covariance matrix is more conservative depends on the type of parameter that we are measuring (see also Hoyle et al. 2018, their appendix A).

Consider two hypothetical parameters to be estimated from a tomographic lensing measurement with two bins, denoted by S (proportional to the sum of amplitudes in the low- and high-redshift bin) and D (proportional to the difference of these amplitudes). Practical examples for S include $S_8 = \sigma_8 \sqrt{\Omega_m / 0.3}$, and for D include photo-z bias parameters of the low- and high-redshift bin. The two most obvious ways to marginalize over m in this scenario are

(i) to marginalize over a single parameter m with Gaussian prior σ_m – this is the same as using a fully correlated m per bin, and

is the most conservative choice possible for S. For D, though, it underestimates the error when m varies with redshift.

(ii) to marginalize over two parameters m_1 and m_2 with fully independent Gaussian priors of width σ_m. This is the most conservative choice for D but underestimates the systematic uncertainty of S due to m by a factor $\sqrt{2}$.

If we want to be conservative for both these types of parameter then we must increase σ_m. If we have n redshift bins with equal signal-to-noise, then we should use uncorrelated m values with $\sigma_{m_i} = \sqrt{N}\sigma_m$. The generalization of this to bins with unequal signal-to-noise ratios ρ_i is to use $\sigma_{m_i} = a \times \sigma_m$ where

$$a = \sqrt{\frac{\sum_{i,j} \rho_i^2 \rho_j^2}{\sum_i \rho_i^4}} . \tag{D1}$$

For cosmic shear and redMaGiC galaxy–galaxy lensing with the binning schemes similar to Troxel et al. (2017) and Prat et al. (2017), we find approximately $a = \sqrt{2.6}$ and $\sqrt{3.1}$, respectively. We take the larger value of a as the default tomographic rescaling of σ_{m_i}.

Analyses using redshift-weighted or binned versions of our shape catalogues should take this re-scaling into account. For METACALIBRATION, it applies to all the contributions to σ_m, and can be multiplied with the $\sigma_m = 0.013$ width. For IM3SHAPE, some of the contributions are either anticorrelated between redshift bins or estimated based on their maximum value among a set of redshift bins, in which case the re-scaling is not necessary. The correct σ_{m_i} is

$$\sigma_{m_i} = \sqrt{0.018^2 + a^2 \times (0.001^2 + 0.004^2 + 0.017^2 + 0.002^2)} . \tag{D2}$$

APPENDIX E: IM3SHAPE FLAGS

IM3SHAPE uses two sets of flags to remove objects. Many of these flags will cause selection biases, so they are also applied in the calibration simulations so that this effect will be taken into account. These flags are described in Tables E1 and E2.

Table E1. IM3SHAPE error flags, for extreme objects. These are not individually propagated into released catalogues.

Value	Meaning
2^0	IM3SHAPE failed completely
2^1	Minimizer failed to converge
2^2	$e < 10^{-4}$: IM3SHAPE fit fail
2^3	e_1 or e_2 outside $(-1, 1)$
2^4	Radius > 20 arcsec
2^5	$R_{gp}/R_p > 6$ or NaN
2^6	Negative or NaN R_{gp}/R_p
2^7	S/N < 1 or NaN
2^8	χ^2 per effective pixel > 3
2^9	Normalized residuals < -20 in any pixel
2^{10}	Normalized residuals > 20 in any pixel
2^{11}	RA more than 10 arcsec from nominal
2^{12}	Dec. more than 10 arcsec from nominal
2^{13}	Failed to measure the FWHM of PSF or galaxy
2^{14}	r-band SEXTRACTOR flag has 0×4 or above

In addition to these flags, the calibration process does not calibrate objects with S/N > 200 or $R_{gp}/R_p > 3$. Objects outside this range have FLAGS_SELECT > 0 in the catalogue.

Table E2. IM3SHAPE info flags, for objects with any undesirable features. These are included in the released catalogues as FLAGS.

Value	Meaning
2^0	Area masked out in the GOLD catalogue
2^1	Region flagged in the GOLD catalogue
2^2	MODEST classifies as star
2^3	Mask fraction > 0.75
2^4	levmar_like_evals > 10 000
2^5	r-band SEXTRACTOR flag 0×1, (bright neighbours)
2^6	r-band SEXTRACTOR flag 0×2, (blending)
2^7	More than 25 per cent of flux masked
2^8	S/N < 12
2^9	S/N > 10000
2^{10}	$R_{gp}/R_p < 1.13$
2^{11}	$R_{gp}/R_p > 3.5$ (very large galaxy)
2^{12}	Radius > 5 arcsec
2^{13}	Radius <0.1 arcsec
2^{14}	Centroid more than 1 arcsec from nominal
2^{15}	χ^2 per effective pixel <0.5
2^{16}	χ^2 per effective pixel > 1.5
2^{17}	Normed residuals <−0.2 somewhere
2^{18}	Normed residuals > 0.2 somewhere
2^{19}	Very large PSF
2^{20}	Negative PSF FWHM
2^{21}	One or more error flags is set

APPENDIX F: METACALIBRATION RESPONSE BEHAVIOUR

The METACALIBRATION response factors R_γ and R_s described in Section 4.1 can vary with any galaxy feature, since they are calculated on a per-object basis. To illustrate the general behaviour of these factors and their relative importance, Fig. F1 shows the size of the different terms. Note that the two quantities plotted are calculated slightly differently – the R_s part is the correction for bias caused by cutting out all objects below the x coordinate value, whereas R_γ is the mean correction for all objects in a bin centred on the x coordinate value.

For the specific estimator chosen here the selection bias associated with signal-to-noise is nearly negligible, being well below 1 per cent, whereas the size selection bias is much larger, peaking at 4 per cent. Our fiducial size cut was $T/T_{PSF} > 0.5$, corresponding to a 2 per cent correction.

Figure F1. Variation of the 1–1 components of the selection bias response correction R_s and mean calibration response $R\gamma$ with signal-to-noise (top) and galaxy size relative to PSF size (bottom).

[1] *Institute for Astronomy, University of Edinburgh, Edinburgh EH9 3HJ, UK*
[2] *Brookhaven National Laboratory, Bldg 510, Upton, NY 11973, USA*
[3] *Jodrell Bank Center for Astrophysics, School of Physics and Astronomy, University of Manchester, Oxford Road, Manchester M13 9PL, UK*
[4] *Center for Cosmology and Astro-Particle Physics, The Ohio State University, Columbus, OH 43210, USA*
[5] *Department of Physics, The Ohio State University, Columbus, OH 43210, USA*
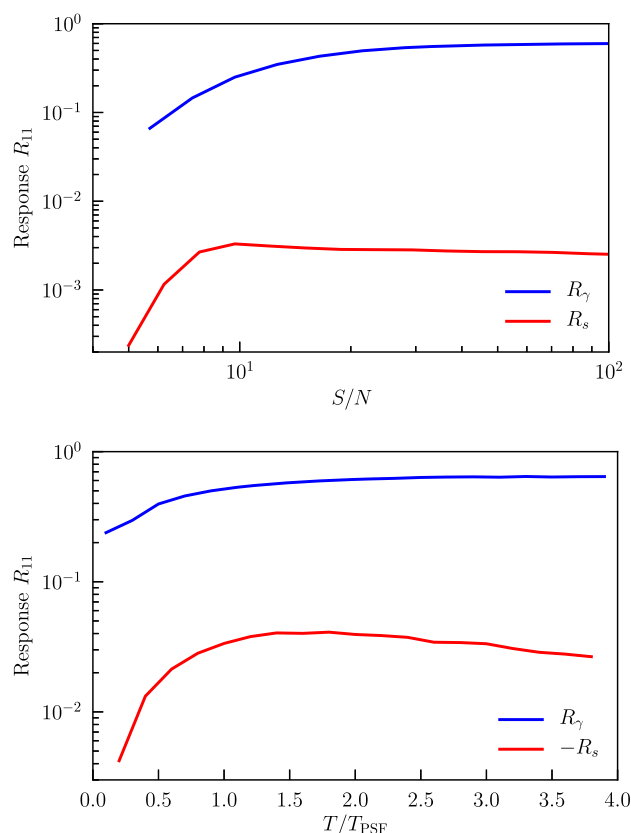[6] *Department of Physics and Astronomy, University of Pennsylvania, Philadelphia, PA 19104, USA*
[7] *Kavli Institute for Particle Astrophysics & Cosmology, PO Box 2450, Stanford University, Stanford, CA 94305, USA*
[8] *SLAC National Accelerator Laboratory, Menlo Park, CA 94025, USA*
[9] *Institut de Física d'Altes Energies (IFAE), The Barcelona Institute of Science and Technology, Campus UAB, E-08193 Bellaterra (Barcelona), Spain*
[10] *Fermi National Accelerator Laboratory, PO Box 500, Batavia, IL 60510, USA*
[11] *Kavli Institute for Cosmological Physics, University of Chicago, Chicago, IL 60637, USA*
[12] *Department of Astronomy, University of Illinois, 1002 W. Green Street, Urbana, IL 61801, USA*
[13] *National Center for Supercomputing Applications, 1205 West Clark St., Urbana, IL 61801, USA*
[14] *Universitäts-Sternwarte, Fakultät für Physik, Ludwig-Maximilians Universität München, Scheinerstr 1, D-81679München, Germany*
[15] *Jet Propulsion Laboratory, California Institute of Technology, 4800 Oak Grove Dr., Pasadena, CA 91109, USA*
[16] *Department of Physics & Astronomy, University College London, Gower Street, London WC1E 6BT, UK*
[17] *Department of Physics, ETH Zurich, Wolfgang-Pauli-Strasse 16, CH-8093 Zurich, Switzerland*
[18] *Centro de Investigaciones Energéticas, Medioambientales y Tecnológicas (CIEMAT), 28040 Madrid, Spain*
[19] *Institute of Astronomy, University of Cambridge, Madingley Road, Cambridge CB3 0HA, UK*
[20] *Kavli Institute for Cosmology, University of Cambridge, Madingley Road, Cambridge CB3 0HA, UK*
[21] *Max Planck Institute for Extraterrestrial Physics, Giessenbachstrasse, D-85748 Garching, Germany*
[22] *Cerro Tololo Inter-American Observatory, National Optical Astronomy Observatory, Casilla 603, La Serena, Chile*
[23] *Department of Physics and Electronics, Rhodes University, PO Box 94, Grahamstown 6140, South Africa*
[24] *LSST, 933 North Cherry Avenue, Tucson, AZ 85721, USA*
[25] *CNRS, UMR 7095, Institut d'Astrophysique de Paris, F-75014 Paris, France*
[26] *Sorbonne Universités, UPMC Univ Paris 06, UMR 7095, Institut d'Astrophysique de Paris, F-75014 Paris, France*
[27] *Laboratório Interinstitucional de e-Astronomia – LIneA, Rua Gal. José Cristino 77, Rio de Janeiro, RJ 20921-400, Brazil*

[28] *Observatório Nacional, Rua Gal. José Cristino 77, Rio de Janeiro, RJ 20921-400, Brazil*

[29] *Institute of Space Sciences, IEEC-CSIC, Campus UAB, Carrer de Can Magrans, s/n, E-08193 Barcelona, Spain*

[30] *Department of Physics, IIT Hyderabad, Kandi, Telangana 502285, India*

[31] *Excellence Cluster Universe, Boltzmannstr 2, D-85748 Garching, Germany*

[32] *Faculty of Physics, Ludwig-Maximilians-Universität, Scheinerstr 1, D-81679 Munich, Germany*

[33] *Department of Physics, California Institute of Technology, Pasadena, CA 91125, USA*

[34] *Department of Astronomy, University of Michigan, Ann Arbor, MI 48109, USA*

[35] *Department of Physics, University of Michigan, Ann Arbor, MI 48109, USA*

[36] *Instituto de Fisica Teorica UAM/CSIC, Universidad Autonoma de Madrid, E-28049 Madrid, Spain*

[37] *Astronomy Department, University of Washington, Box 351580, Seattle, WA 98195, USA*

[38] *Santa Cruz Institute for Particle Physics, Santa Cruz, CA 95064, USA*

[39] *Australian Astronomical Observatory, North Ryde, NSW 2113, Australia*

[40] *Argonne National Laboratory, 9700 South Cass Avenue, Lemont, IL 60439, USA*

[41] *Departamento de Física Matemática, Instituto de Física, Universidade de São Paulo, CP 66318, São Paulo, SP 05314-970, Brazil*

[42] *Department of Astronomy, The Ohio State University, Columbus, OH 43210, USA*

[43] *Department of Astrophysical Sciences, Princeton University, Peyton Hall, Princeton, NJ 08544, USA*

[44] *Institució Catalana de Recerca i Estudis Avançats, E-08010 Barcelona, Spain*

[45] *Institute of Cosmology & Gravitation, University of Portsmouth, Portsmouth PO1 3FX, UK*

[46] *Lawrence Berkeley National Laboratory, 1 Cyclotron Road, Berkeley, CA 94720, USA*

[47] *Department of Physics and Astronomy, Pevensey Building, University of Sussex, Brighton BN1 9QH, UK*

[48] *School of Physics and Astronomy, University of Southampton, Southampton SO17 1BJ, UK*

[49] *Instituto de Física Gleb Wataghin, Universidade Estadual de Campinas, 13083-859 Campinas, SP, Brazil*

[50] *Computer Science and Mathematics Division, Oak Ridge National Laboratory, Oak Ridge, TN 37831, USA*

[51] *Department of Physics, Stanford University, 382 Via Pueblo Mall, Stanford, CA 94305, USA*

This paper has been typeset from a TEX/LATEX file prepared by the author.